

Measurement of $e^+e^- \rightarrow \omega\pi^+\pi^-$ cross section at $\sqrt{s} = 2.000$ to 3.080 GeV

ABSTRACT: Using 647 pb^{-1} of data sample collected with the BESIII detector operating at the BEPCII storage ring at center-of-mass energies from 2.000 GeV to 3.080 GeV, a partial-wave analysis is performed for the process $e^+e^- \rightarrow \omega\pi^+\pi^-$. The Born cross section of the process $e^+e^- \rightarrow \omega\pi^+\pi^-$ is measured with precision improved by a factor of 3. A structure near 2.25 GeV is observed in the energy dependent cross sections of $e^+e^- \rightarrow \omega\pi^+\pi^-$ and $\omega\pi^0\pi^0$ with a statistical significance of 7.6σ , and its mass and width are determined to be $2232 \pm 19 \pm 27 \text{ MeV}/c^2$ and width $93 \pm 53 \pm 20 \text{ MeV}$, respectively, where the first uncertainties are statistical and the second ones are systematic. By analyzing the cross sections of the subprocesses $e^+e^- \rightarrow \omega f_0(500)$, $\omega f_0(980)$, $\omega f_0(1370)$, $\omega f_2(1270)$ and $b_1(1235)\pi$, a structure with mass $M = (2200 \pm 11 \pm 17) \text{ MeV}/c^2$ and width $\Gamma = (74 \pm 20 \pm 24) \text{ MeV}$, is observed with a combined significance of 7.9σ . The measured resonance parameters will help to reveal the nature of the vector states around 2.2 GeV.

Contents

1	Introduction	1
2	BESIII detector and Monte Carlo simulation	2
3	Event selection and background analysis	3
4	Amplitude analysis	4
4.1	Kinematic variable	4
4.2	Decay amplitude	5
4.3	Simultaneous fit	7
4.4	Intermediate states and significance check	8
4.5	Fit results	9
5	Born cross section	9
5.1	ISR correction factor	9
5.2	Cross section for $e^+e^- \rightarrow \omega\pi^+\pi^-$	13
5.3	Cross sections for the intermediate subprocesses	14
6	Systematic uncertainties	15
6.1	Uncertainties for intermediate subprocesses	15
6.2	Uncertainties for measurements of $\sigma(e^+e^- \rightarrow \omega\pi^+\pi^-)$	17
7	Fit to the line shapes	19
7.1	Line shape of $e^+e^- \rightarrow \omega\pi^+\pi^-$	19
7.2	Cross section of $e^+e^- \rightarrow \omega\pi\pi$	20
7.3	The $X(2230)$ decays via intermediate states	22
8	Conclusion and discussion	23
9	Acknowledgments	25

1 Introduction

Electron-positron annihilation at fixed center-of-mass (c.m.) energies has long been a mainstay of research in elementary particle physics. Search for exotic hadronic states in the electron-positron collider experiments has been continuously received much attention for many years. Some exciting observations have been reported from the e^+e^- experiments [1–12]. The measurements of the exclusive decay cross sections are of particular interest for resolving the discrepancy of muon magnetic anomaly $a_\mu = (g_\mu - 2)/2$ between the measurement and the standard model (SM) prediction. The latest result by the Fermi National

Accelerator Laboratory (FNAL) of Muon $g - 2$ Experiment showing 4.2 standard deviation greater than the SM prediction [13], gives a strong hint for the existence of new physics [14]. To confirm this, however, further improvements in the precision for both experimental measurement and theoretical prediction are necessary. Especially, the precision measurements on the cross sections of light hadrons production in the e^+e^- annihilation are essential to reduce the uncertainty of theoretical estimation on the hadronic vacuum polarization contribution to the muon anomaly a_μ [15].

The BaBar experiment has studied this process using the initial state radiation (ISR) method [16], and an indication of an isoscalar resonance structure near 2.25 GeV was seen in the line shape of $e^+e^- \rightarrow \omega\pi^+\pi^-$ [17]. However, due to limited statistic, the BaBar experiment did not determine the yields of intermediate states except for the decay $e^+e^- \rightarrow \omega f_0(980)$ in the process, and resonance parameters of the structure near 2.25 GeV except for its mass and width [17]. The systems $\omega f_0(500)$, $\omega f_0(980)$, $\omega f_0(1370)$, and $\omega f_2(1270)$ have isospin zero, which is useful to search for excited ω and ϕ states, and important to confirm the structure near 2.25 GeV observed by the BaBar experiment [17]. This structure may be corresponding to the resonances $\phi(2170)$, $\omega(2205)$, $\omega(2290)$ and $\omega(2330)$, whose properties are poorly known in Particle Data Group (PDG) [18]. Many interpretations have been proposed for the $\phi(2170)$, including a traditional $s\bar{s}$ state [19–24], a $s\bar{s}g$ hybrid [25, 26], a $ss\bar{s}\bar{d}$ tetraquark state [27–34], a $\Lambda\bar{\Lambda}$ bound state [35–39] or an ordinary resonant state of $\phi f_0(980)$ produced by interactions between the final state particles [40, 41]. Recently, the $\phi(2170)$ state has been studied by the BESIII experiment in the processes of $e^+e^- \rightarrow K^+K^-$ [42], $K^+K^-\pi^0\pi^0$ [43], $\phi\eta'$ [44], $\omega\eta$ [45], $K_S^0K_L^0$ [46], $\phi\eta$ [47] and $2(K^+K^-)$, ϕK^+K^- [48]. The decay properties of $\omega(2205)$ as a candidate of $\omega(3D)$, $\omega(2290)$ and $\omega(2330)$ as candidates of $\omega(4S)$ states have been discussed [49]. Further experimental studies of the decay properties of these resonances are highly desired to reveal their natures.

In this paper, we report a measurement of Born cross section for the process $e^+e^- \rightarrow \omega\pi^+\pi^-$ using the data collected in an energy scan at nineteen energies from 2.000 GeV to 3.080 GeV with a total integrated luminosity of 647 pb $^{-1}$, where the detailed values of c.m. energy and integrated luminosities of each data set are presented in Section 5.2. Combined with the measurements of $e^+e^- \rightarrow \omega\pi^+\pi^-$ and the previous $e^+e^- \rightarrow \omega\pi^0\pi^0$ [50], the cross sections of $e^+e^- \rightarrow \omega\pi\pi$ are also obtained. With an amplitude analysis, the cross sections of the subprocesses via intermediate states, e.g., $e^+e^- \rightarrow \omega f_0(500)$, $\omega f_0(980)$, $\omega f_0(1370)$, $\omega f_2(1270)$ and $b_1(1235)\pi$ are determined.

2 BESIII detector and Monte Carlo simulation

The BESIII detector [51] records symmetric e^+e^- collisions provided by the BEPCII storage ring [52], which operates in the center-of-mass energy range from 2.000 GeV to 4.950 GeV [53]. BESIII has collected large data samples in this energy region [54]. The cylindrical core of the BESIII detector covers 93% of the full solid angle and consists of a helium-based multi-layer drift chamber (MDC), a plastic scintillator time-of-flight system (TOF), and a CsI(Tl) electromagnetic calorimeter (EMC), which are all enclosed in a superconducting solenoidal

magnet providing a 1.0 T (0.9 T in 2012) magnetic field. The solenoid is supported by an octagonal flux-return yoke with resistive plate counter muon identification modules interleaved with steel. The charged-particle momentum resolution at 1 GeV/c is 0.5%, and the dE/dx resolution is 6% for electrons from Bhabha scattering. The EMC measures photon energies with a resolution of 2.5% (5%) at 1 GeV in the barrel (end cap) region. The time resolution in the TOF barrel region is 68 ps, while that in the end cap region is 110 ps.

Monte-Carlo (MC) events are produced with the GEANT4-based [55] offline software BOSS [51], including the geometric description of the BESIII detector and the detector response. Two millions of inclusive MC events, $e^+e^- \rightarrow$ hadrons, are used to estimate the background contamination. They are generated using the hybrid generator, which integrates PHOKARA [56, 57], CONEXC [58, 59] and LUARLW [60] models. The model PHOKARA generates ten well parameterized and established exclusive channels. The CONEXC model simulates a total of 47 exclusive processes according to a homogeneous and isotropic phase space population and reproduces the measured line shapes of the absolute cross section. And the remaining unknown decays of the virtual photon are modeled by the LUARLW model.

Signal MC events for $e^+e^- \rightarrow \omega\pi^+\pi^-$ are generated by using the amplitude model with parameters fixed to the helicity amplitude analysis results, and the significant intermediate states are included with the initial state radiation effects.

3 Event selection and background analysis

A data sample of $e^+e^- \rightarrow \pi^+\pi^-\pi^+\pi^-\pi^0$ is selected by requiring the net charge zero of four charged tracks and at least two photons. Charged tracks detected in the MDC are required to be within a polar angle (θ) range of $|\cos\theta| < 0.93$, where θ is defined with respect to the beam direction. For charged tracks, the distance of closest approach to the interaction point (IP) must be less than 10 cm along the symmetry axis of the MDC, $|V_z|$, and less than 1 cm in the transverse plane, $|V_{xy}|$. Photon candidates are identified using showers in the EMC. The deposited energy of each shower is more than 25 MeV in the barrel region ($|\cos\theta| < 0.80$) and more than 50 MeV in the end cap region ($0.86 < |\cos\theta| < 0.92$). To exclude showers that originate from charged tracks, the angle between the position of each shower in the EMC and the closest extrapolated charged track is greater than 10 degrees. To suppress electronic noise and showers unrelated to the event, the difference between the EMC time and the event start time is required to be within (0, 700) ns.

To improve the mass resolution and suppress the background contribution, a four-constrain (4C) kinematic fit is performed under the hypothesis of $e^+e^- \rightarrow 2(\pi^+\pi^-)\gamma\gamma$ to constrain the sum of four momentum of the final state particles to the initial colliding beams. If there are more than two photons, the combination with minimum χ_{4C}^2 is kept for further analysis. Based on an optimization of $\frac{N_s}{\sqrt{(N_s+N_b)}}$ for the requirement on χ_{4C}^2 , where N_s and $N_s + N_b$ is the number of events in the ω signal region for signal MC and data, respectively, candidate events with $\chi_{4C}^2 < 40$ are accepted for further analysis. The $\omega\pi^+\pi^-$ events are selected by requiring that the ω candidates are reconstructed out of all the four $\pi^+\pi^-\pi^0$ combinations with minimal mass difference from the ω known mass [18]. The π^0

candidate is reconstructed by the $\gamma\gamma$ combination with a mass window $0.12 < M_{\gamma\gamma} < 0.15$ GeV/c^2 , and the ω signal region is defined with a requirement of $0.758 < M_{\pi^+\pi^-\pi^0} < 0.808$ GeV/c^2 . To estimate background, the ω sidebands are defined as $[0.733, 0.758]$ GeV/c^2 and $[0.808, 0.833]$ GeV/c^2 . The $e^+e^- \rightarrow \pi^+\pi^-\pi^+\pi^-\pi^0$ process is found to be the dominant background source by analysing the inclusive MC sample with the help of a generic event type analysis tool, TopoAna [61]. No peaking background is found in the signal region.

The selection of 3π combination for the ω candidate may lead to the wrong $\pi^+\pi^-\pi^0$ combination. The ratio due to the mis-combination is carefully studied by matching the production of ω MC event. Using a sample containing 0.5 million MC events of the $e^+e^- \rightarrow 2(\pi^+\pi^-\pi^0)$ decay, a full truth MC matches on MDC/EMC track level of all final state particles. As a event is marked as "mis-combination", when a charged pion is assigned to be from the wrong ω candidate. The ratio of the number of mis-combination ω to total number of events is about 1.0% on the average. The mis-combination yields will be subtracted from the ω candidate events when calculating the $e^+e^- \rightarrow \omega\pi^+\pi^-$ Born cross section.

4 Amplitude analysis

4.1 Kinematic variable

At e^+e^- collider, the $\omega\pi^+\pi^-$ events selected with the kinematic constraints are produced from the e^+e^- annihilation into a virtual photon, then transforms to light quarks, followed by hadronization into the $\pi^+(p_1)\pi^-(p_2)\omega(p_3)$ final states, where p_i ($i = 1, 2, 3$) denote the momentum reconstructed for the associated particles. In the process $e^+e^- \rightarrow \omega\pi^+\pi^-$, we measure the Born cross section for the processes as shown in Fig. 1 (a) for $e^+e^- \rightarrow R_1\omega$, $R_1 \rightarrow \pi\pi$, (b) for $e^+e^- \rightarrow \pi^-R_2^+$, $R_2^+ \rightarrow \pi^+\omega$ and (c) for $e^+e^- \rightarrow \pi^+R_2^-$, $R_2^- \rightarrow \pi^-\omega$, where R_1 and R_2^\pm denote intermediate states. In the amplitude analysis, intensity for each

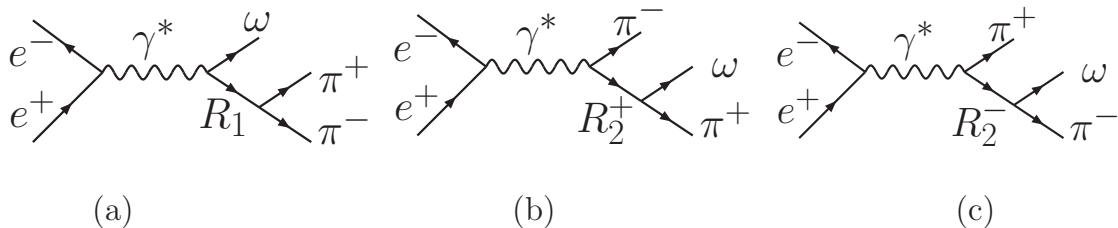


Figure 1. The quasi-two body decays in the process $e^+e^- \rightarrow \omega\pi^+\pi^-$.

Born process is described with the helicity amplitude, which is constructed as the amplitude production of two sequential decays in the helicity frame. Taking process (a) as an example of helicity rotation angles (see Fig. 2), the R_1 polar angle, $\theta_{[12]}^{[123]}$, is defined as the angle spanned between the R_1 momentum and the positron moving direction, the azimuthal angle $\phi_{[12]}^{[123]}$ is the angle between the R_1 production plane and its decay plane and for the $R_1 \rightarrow \pi^+\pi^-$ decay, the azimuthal angle, $\phi_{[1]}^{[12]}$, is defined as the angle between R_1 production

plane and its decay plane, formed by the $\pi^+\pi^-$ momentum. After boosting the two pion momenta to the R_1 rest frame, they still locate in the same decay plane. The polar angle $\theta_{[1]}^{[12]}$ for π^+ is defined as the angle between the $\pi^+\pi^-$ and R_1 momentum in the R_1 rest frame. Helicity angles for process (b) and (c) are defined in the same way. Table 1 lists the definitions of helicity angles and amplitudes for the three processes.

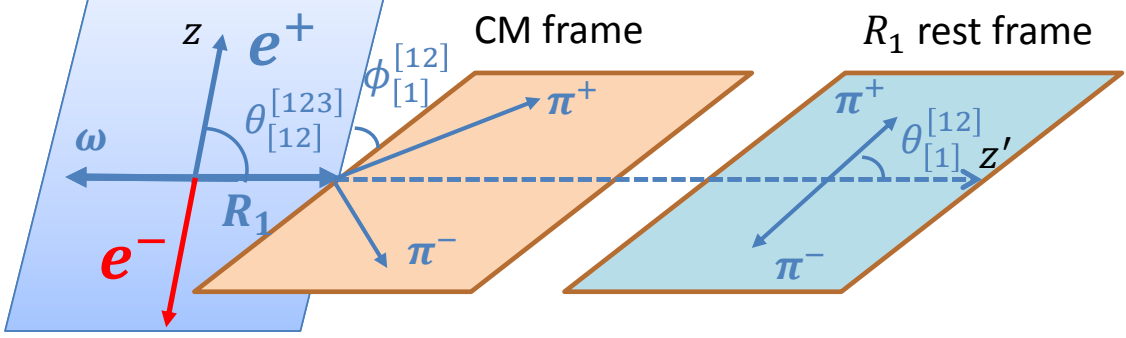


Figure 2. Helicity rotation angles defined for the process $e^+e^- \rightarrow R_1\omega$, $R_1 \rightarrow \pi^+\pi^-$.

Table 1. Definitions of helicity angles and amplitudes for the sequential decays (a), (b) and (c). The λ_i and m denote the helicity values for corresponding particle and the spin z projection of virtual photon in electron-positron annihilation.

Decay processes	Helicity angles	Amplitudes
$e^+e^- \rightarrow \gamma^*(m) \rightarrow R_1(\lambda_R)\omega(\lambda_3)$	$\theta_{[12]}^{[123]}, \phi_{[12]}^{[123]}$	$F_{\lambda_R, \lambda_3}^{\gamma^*}$
$R_1 \rightarrow \pi^+\pi^-$	$\theta_{[1]}^{[12]}, \phi_{[1]}^{[12]}$	$F_{0,0}^{R_1}$
$e^+e^- \rightarrow \gamma^*(m) \rightarrow R_2^+(\lambda_+)\pi^-$	$\theta_{[13]}^{[123]}, \phi_{[13]}^{[123]}$	$F_{\lambda_+, 0}^{\gamma^*}$
$R_2^+ \rightarrow \omega(\lambda'_3)\pi^+$	$\theta_{[3]}^{[13]}, \phi_{[3]}^{[13]}$	$F_{\lambda'_3, 0}^{R_2^+}$
$e^+e^- \rightarrow \gamma^*(m) \rightarrow R_2^-(\lambda_-)\pi^+$	$\theta_{[23]}^{[123]}, \phi_{[23]}^{[123]}$	$F_{\lambda_-, 0}^{\gamma^*}$
$R_2^- \rightarrow \omega(\lambda''_3)\pi^-$	$\theta_{[3]}^{[23]}, \phi_{[3]}^{[23]}$	$F_{\lambda''_3, 0}^{R_2^-}$

4.2 Decay amplitude

Decay amplitude for process (a) reads

$$A_1(m, \lambda_3) = \sum_{\lambda_R} F_{\lambda_R, \lambda_3}^{\gamma^*} D_{m, \lambda_R - \lambda_3}^{1*}(\phi_{[12]}^{[123]}, \theta_{[12]}^{[123]}, 0) BW(m_{12}) F_{0,0}^{R_1} D_{\lambda_R, 0}^{J*}(\phi_{[1]}^{[12]}, \theta_{[1]}^{[12]}, 0), \quad (4.1)$$

where $D_{m, \lambda}^J(\phi, \theta, 0)$ is Wigner- D function, J is the spin of resonance R_1 , and BW denotes Breit-Wigner function.

Decay amplitude for process (b) reads

$$A_2(m, \lambda_3) = \sum_{\lambda_+, \lambda'_3} F_{\lambda_+, 0}^{\gamma^*} D_{m, \lambda_+}^{1*}(\phi_{[13]}^{[123]}, \theta_{[13]}^{[123]}, 0) BW(m_{13}) F_{\lambda'_3, 0}^{R_2^+} D_{\lambda_+, \lambda'_3}^{J*}(\phi_{[3]}^{[13]}, \theta_{[3]}^{[13]}, 0) \times D_{\lambda'_3, \lambda_3}^1(\phi'_3, \theta'_3, 0), \quad (4.2)$$

where J is the spin of R_2^+ . Since the ω helicity defined in this process is different from that defined in process (a). One needs to perform a rotation to align the ω helicity to coincide with that in the process (a) by the angle (θ'_3, ϕ'_3) . This issue has been addressed in the analyses [62, 63] and proved in Ref. [64].

Decay amplitude for process (c) reads

$$A_3(m, \lambda_3) = \sum_{\lambda_-, \lambda'_3} F_{\lambda_-, 0}^{\gamma^*} D_{m, \lambda_-}^{1*}(\phi_{[23]}^{[123]}, \theta_{[23]}^{[123]}, 0) BW(m_{23}) F_{\lambda'_3, 0}^{R_2^-} D_{\lambda_-, \lambda'_3}^{J*}(\phi_{[3]}^{[23]}, \theta_{[3]}^{[23]}, 0) \times D_{\lambda'_3, \lambda_3}^1(\phi''_3, \theta''_3, 0), \quad (4.3)$$

where J is the spin of R_2^- . And the Wigner function $D_{\lambda'_3, \lambda_3}^J(\phi''_3, \theta''_3, 0)$ is used to align the ω helicity to coincide with that defined in the process (a).

The nonresonant three-body decay $e^+e^- \rightarrow \omega\pi^+\pi^-$ is also taken into account, and its amplitude is written as [65–68]:

$$A_4(m, \lambda_3) = \sum_{\mu} F_{\mu, \lambda_3} D_{m, \mu}^{1*}(\alpha, \beta, \gamma), \quad (4.4)$$

where μ is the z -component of spin J in the helicity system, $m(\lambda_3)$ is the helicity value for $\gamma^*(\omega)$. α, β, γ are the Euler angles as defined in Refs. [65–68]. F_{μ, λ_3} is the helicity amplitude. The decay conserves the parity, thus leads to $F_{\pm, \lambda_3} = -F_{\pm, -\lambda_3}$ and $F_{0, \lambda_3} = F_{0, -\lambda_3}$.

To match the covariant tensor amplitude, we expand the helicity amplitude in terms of the partial waves for the two-body decay in LS -coupling scheme [66–68]. It follows

$$F_{\lambda, \nu}^J = \sum_{lS} \left(\frac{2l+1}{2J+1} \right)^{1/2} \langle l0S\delta | J\delta \rangle \langle s\lambda\sigma - \nu | S\delta \rangle g_{lS} r^l \frac{B_l(r)}{B_l(r_0)}, \quad (4.5)$$

for a spin- J particle decay $J \rightarrow s + \sigma$, λ and ν are the helicities of two final-state particles s and σ with $\delta = \lambda - \nu$. The symbol g_{lS} is a coupling constant, S is the total intrinsic spin $\mathbf{S} = \mathbf{s} + \boldsymbol{\sigma}$, l is the orbital angular momentum, $r = |\mathbf{r}|$, where \mathbf{r} is the relative momentum between the two daughter particles in their mother rest frame, \mathbf{r}_0 corresponds to the invariant mass of the resonance equal to its nominal mass. The Blatt-Weisskopf factor

$B_l(r)$ [66–68] up to $l = 4$ takes the form as

$$\begin{aligned}
B_0(r)/B_0(r_0) &= 1, \\
B_1(r)/B_1(r_0) &= \frac{\sqrt{1 + (dr)^2}}{\sqrt{1 + (dr_0)^2}}, \\
B_2(r)/B_2(r_0) &= \frac{\sqrt{9 + 3(dr)^2 + (dr)^4}}{\sqrt{9 + 3(dr_0)^2 + (dr_0)^4}}, \\
B_3(r)/B_3(r_0) &= \frac{\sqrt{225 + 45(dr)^2 + 6(dr)^4 + (dr)^6}}{\sqrt{225 + 45(dr_0)^2 + 6(dr_0)^4 + (dr_0)^6}}, \\
B_4(r)/B_4(r_0) &= \frac{\sqrt{11025 + 1575(dr)^2 + 135(dr)^4 + 10(dr)^6 + (dr)^8}}{\sqrt{11025 + 1575(dr_0)^2 + 135(dr_0)^4 + 10(dr_0)^6 + (dr_0)^8}},
\end{aligned} \tag{4.6}$$

where the parameter d is constant fixed to 3 GeV^{-1} [62].

The differential cross section is given by

$$d\sigma = \frac{1}{2} \sum_{m, \lambda_3} \Omega(\lambda_3) \left| \sum_{i=1}^3 A_i(m, \lambda_3) \right|^2 d\Phi, \tag{4.7}$$

where $m = \pm 1$ is due to the virtual photon produced from unpolarized e^+e^- annihilations, λ_3 is the ω helicity value and $d\Phi$ is the element of standard three-body phase space. The variable $\Omega(\lambda_3) (= |\varepsilon(\lambda_3) \cdot (\mathbf{q}_1 \times \mathbf{q}_2)|^2)$ is the ω decay matrix into the $\pi^+\pi^-$ final states, where ε is the ω polarization vector, and $\mathbf{q}_1(\mathbf{q}_2)$ is the momentum vector for $\pi^+(\pi^-)$ from the ω decay. Here we factor out the Breit-Wigner function describing the ω line shape into the MC integration when applying the amplitude model fit to the data events.

4.3 Simultaneous fit

The relative magnitudes and phases for coupling constants are determined by an unbinned maximum likelihood fit. The joint probability density for observing N events in one data set is

$$\mathcal{L} = \prod_{i=1}^N P_i(p_1, p_2, p_3, p_4, p_5), \tag{4.8}$$

where p_i ($i = 1, 2, \dots, 5$) denotes the four-vector momenta of final states, and P_i is a probability to produce event i with the momenta of final states. The normalized P_i is calculated from the differential cross section

$$P_i = \frac{(d\sigma/d\Phi)_i}{\sigma_{\text{MC}}}, \tag{4.9}$$

where the normalization factor σ_{MC} is calculated using a signal MC sample with N_{MC} accepted events, which are generated with a uniform distribution in phase space and subjected to the detector simulation, and then are passed through the same event selection criteria as applied to the data events. With a MC sample of two million events, the σ_{MC} is well approximately evaluated with

$$\sigma_{\text{MC}} \approx \frac{1}{N_{\text{MC}}} \sum_{i=1}^{N_{\text{MC}}} \left(\frac{d\sigma}{d\Phi} \right)_i. \tag{4.10}$$

For technical reasons, rather than maximizing \mathcal{L} , the object function, $S = -\ln \mathcal{L}$, is minimized using MINUIT [69]. To subtract the background events, the $\ln \mathcal{L}$ function is replaced with

$$S = -\ln \mathcal{L} = -(\ln \mathcal{L}_{\text{data}} - \ln \mathcal{L}_{\text{bg}}), \quad (4.11)$$

Where $\mathcal{L}_{\text{data}}$ and \mathcal{L}_{bg} are the joint probability densities for data and background, respectively. The background events are obtained by the normalized ω sidebands.

We perform a simultaneous fit to an ensemble of the $\omega\pi^+\pi^-$ events with different c.m. energies, and their amplitudes share same coupling constants describing the intermediate state decays. The total object function is taken as the sum of individual ones, i.e.,

$$S' = -\sum_{j=1}^N \ln \mathcal{L}_j, \quad (4.12)$$

for the total N sets of data events.

After the parameters are determined in the fit, the signal yield of a given subprocess can be estimated by scaling its cross section ratio r_i to the number of net events

$$N_i = r_i(N_{\text{obs}} - N_{\text{bg}}), \quad \text{with } r_i = \frac{\sigma_i}{\sigma_{\text{tot}}}, \quad (4.13)$$

where σ_i is the cross section for the i -th subprocess as defined in Eq.(4.7), σ_{tot} is the total cross section, N_{obs} is the number of observed events and N_{bg} is the number of background events.

The statistical uncertainty, δN_i , associated with signal yield N_i is estimated according to the error propagation formula using the covariance matrix V , obtained from the fit, namely

$$\delta N_i^2 = \sum_{m=1}^{N_{\text{pars}}} \sum_{n=1}^{N_{\text{pars}}} \left(\frac{\partial N_i}{\partial X_m} \frac{\partial N_i}{\partial X_n} \right)_{\mathbf{X}=\mu} V_{mn}(\mathbf{X}), \quad (4.14)$$

where \mathbf{X} is a vector containing parameters, and μ contains the fitted values for all parameters. The sum runs over all N_{pars} parameters.

4.4 Intermediate states and significance check

In term of the $\pi^+\pi^-$ mass spectrum of Fig. 3, the $f_0(980)$ signals are significantly observed in the data events with e^+e^- c.m. energies below 2.300 GeV. In the low $\pi^+\pi^-$ energy region, the $f_0(500)$ resonance may have some contributions, and in the high energy region, the $f_0(1370)$ and $f_2(1270)$ resonances are included in the amplitude model. The $f_0(980)$ line shape is parameterized with Flattê formula:

$$BW(s) = \frac{1}{s - m_0^2 + i(g_1\rho_{\pi\pi}(s) + g_2\rho_{K\bar{K}}(s))}, \quad (4.15)$$

where $\rho(s) = 2k/\sqrt{s}$, k is the c.m. momentum of the π or K in the resonance rest frame, g_1 and $\frac{g_2}{g_1}$ are fixed to the measured values $0.138 \pm 0.010 \text{ GeV}^2$ and 4.45 ± 0.25 , respectively [70, 71], and m_0 is the mass of the resonance $f_0(980)$ ($m_0=0.990 \text{ GeV}/c^2$).

For the $f_0(500)$ line shape, there are many types of energy-dependence-width parameterizations in literature [70, 71], and we choose the E791 parameterizations (used by the E791 Collaboration) in the nominal fit, i.e.

$$BW(s) = \frac{1}{s - m_0^2 + i\sqrt{s}\Gamma}, \text{ with } \Gamma = \sqrt{1 - \frac{4m_\pi^2}{s}}\Gamma_0, \quad (4.16)$$

where m_0 and Γ_0 are the $f_0(500)$ mass and width, respectively. For the other resonances, such as $f_0(1370)$, $f_2(1270)$, $b_1(1235)$ and so on, the width is taken as the constant width. The line shape is described with the Breit-Weigner function.

In the mass spectrum of $\omega\pi^\pm$, the isospin-vector resonances, $b_1(1235)$, $\rho(1450)^\pm$ and $\rho(1570)^\pm$, are included in the significance test, and their line shapes are parameterized with a constant width of Breit-Wigner function, with masses and widths fixed to the PDG values.

The above fitting strategy is implemented individually on the data sets collected $\sqrt{s} = 2.125$ GeV and 2.396 GeV, which have the largest luminosities and yields among the nineteen datasets. The other seventeen data samples have limited statistics, so they are fitted using the resonances from the baseline solutions obtained with $\sqrt{s} = 2.125$ GeV (for $\sqrt{s} = 2.000, 2.100, 2.175, 2.200$ and 2.232 GeV, hereafter called group A) and $\sqrt{s} = 2.396$ GeV (for other data samples, hereafter named group B).

Taking the fact into account that the cross section of these intermediate states may vary with the c.m. energy \sqrt{s} , the constants responsible for the virtual photon γ^* coupling to a given state are allowed to float when fitting to data set at different energy point, while coupling constants for the subsequent decay are taken as the common parameters, which are shared in the fit to all the data set. The masses, widths and the Flatté parameters for the resonances are fixed to the measured values as given in Table 2.

The statistical significance of each amplitude is evaluated by incorporating the change in likelihood and degree of freedom fits with and without the corresponding amplitude included in the simultaneous fit. The significance for each state is given in Table 2. We take the subprocess with the significance greater than 5σ in group A and group B data sets to be the baseline solutions, which include $e^+e^- \rightarrow \omega f_0(500), \omega f_0(980), \omega f_0(1370), \omega f_2(1270)$ and $b_1^\mp(1235)\pi^\pm$.

4.5 Fit results

Signal yields for data sets are calculated with Eq. (4.13), and their statistical uncertainties are derived according to Eq. (4.14), which include the correlation among parameters. Signal yields are given in Table 3. Projections of invariant masses for individual energy points are shown in Fig. 3. The combined energy points of mass projections of fit results for group A and group B are shown in Fig. 4 and Fig. 5, respectively.

5 Born cross section

5.1 ISR correction factor

In the direct e^+e^- experiments, the observed cross section, $\sigma_{\text{obs}}(s)$, at c.m. energy point \sqrt{s} for $e^+e^- \rightarrow \omega\pi^+\pi^-$ is the Born cross section, $\sigma_0(s)$, convolved with the initial state

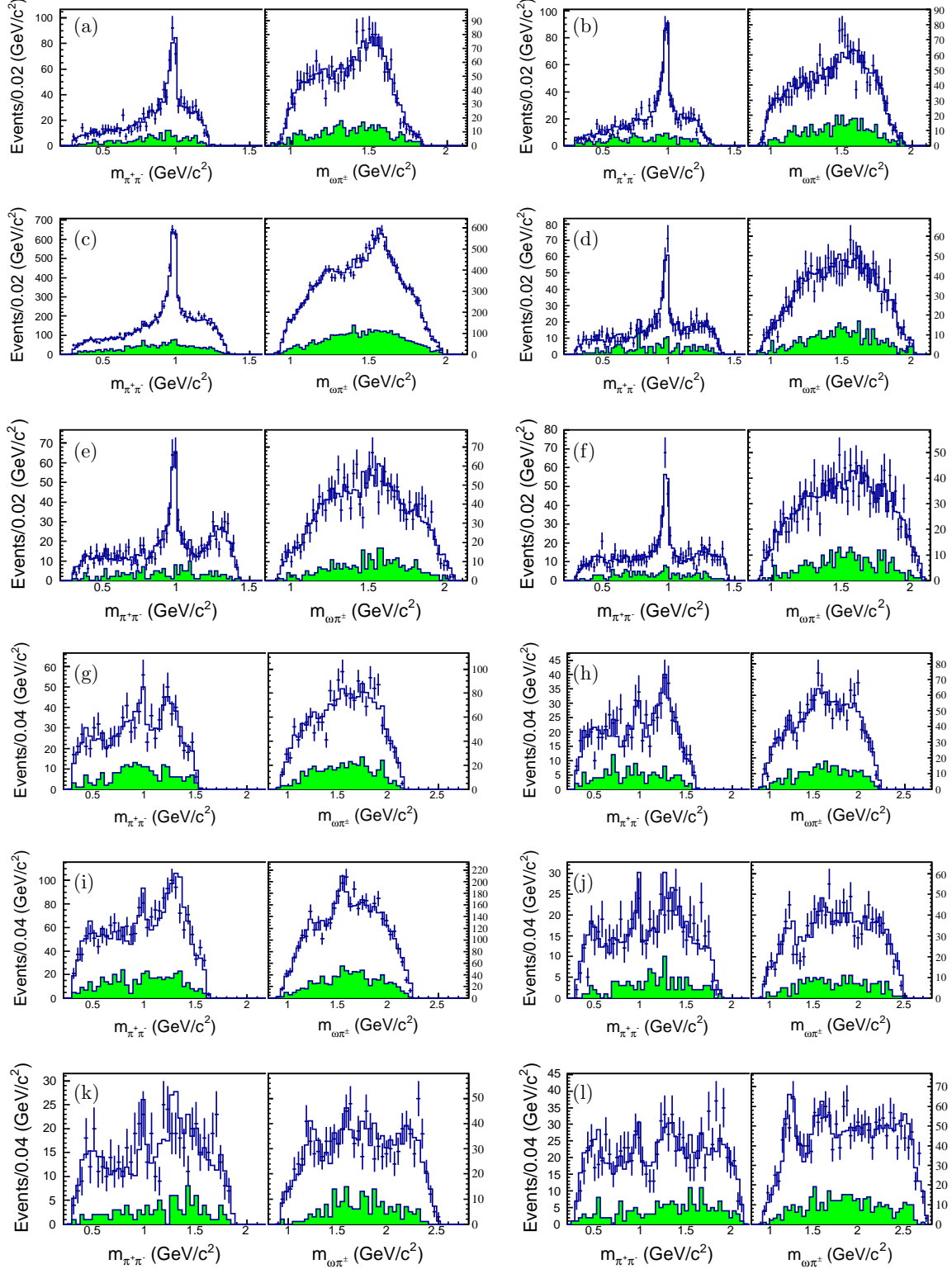


Figure 3. Projections of fit results for mass spectra $m_{\pi^+\pi^-}$ and $m_{\omega\pi^\pm}$ for various energy points. Dots with error bars are data, histograms are the projection of fit results, and shaded histograms (green) are the background estimated by the ω mass sideband. The subplots are (a) for 2.0000 GeV, (b) for 2.1000 GeV, (c) for 2.1250 GeV, (d) for 2.1750 GeV, (e) for 2.2000 GeV, (f) for 2.1750 GeV, (g) for 2.3094 GeV, (h) for 2.3864 GeV, (i) for 2.3960 GeV, (j) for 2.6444 GeV, (k) for 2.6464 GeV and (l) for 2.9000 GeV.

Table 2. Masses and widths of the intermediate states and the statistical significances of corresponding intermediate processes in the data sets of group A ($\sqrt{s} = 2.0000 \sim 2.2324$) and group B ($\sqrt{s} = 2.3094 \sim 2.9000$ GeV).

Resonance	Mass (GeV/ c^2)	Width (GeV)	Group A	Group B
$f_0(500)$	0.507 (0.400~0.550)	0.475 (0.400~0.700)	8.4σ	14.0σ
$f_0(980)$	0.990 ± 0.020	—	15.0σ	11.8σ
$f_0(1370)$	1.350 ± 0.050	0.200 ± 0.500	12.6σ	9.1σ
$f_2(1270)$	1.2755 ± 0.0008	0.1867 ± 0.0022	12.6σ	11.0σ
$b_1^\pm(1235)$	1.2295 ± 0.0032	0.142 ± 0.009	11.1σ	19.0σ
$\rho(1450)^\pm$	1.465 ± 0.025	0.400 ± 0.060	4.4σ	8.3σ
$\rho(1570)^\pm$	1.570 ± 0.070	0.144 ± 0.090	6.1σ	4.3σ

Table 3. Signal yields of the subprocesses at each energy point, where the uncertainties are only statistical. Where the last column means the non-resonance part.

\sqrt{s} (GeV)	$\omega f_0(500)$	$\omega f_0(980)$	$\omega f_0(1370)$	$\omega f_2(1270)$	$b_1^\mp(1235)\pi^\pm$	$\omega\pi^+\pi^-$
2.0000	58.6 ± 23.6	446.4 ± 42.4	200.4 ± 50.3	167.2 ± 26.8	27.8 ± 8.9	1.1 ± 0.1
2.1000	45.1 ± 19.9	578.4 ± 46.7	197.6 ± 46.3	130.0 ± 25.1	9.3 ± 6.6	10.9 ± 10.1
2.1250	720.2 ± 76.9	$2281. \pm 104.8$	787.2 ± 117.8	759.5 ± 85.6	316.0 ± 41.1	24.6 ± 1.1
2.1750	130.3 ± 23.7	242.9 ± 29.7	59.0 ± 24.5	57.1 ± 20.3	55.4 ± 11.5	15.4 ± 8.1
2.2000	98.5 ± 20.7	262.9 ± 31.1	305.7 ± 47.0	146.7 ± 30.5	13.3 ± 7.8	13.0 ± 10.3
2.2324	100.5 ± 15.7	242.8 ± 25.7	187.7 ± 33.9	50.5 ± 14.6	23.9 ± 8.9	64.0 ± 8.8
2.3094	205.4 ± 41.7	63.0 ± 24.8	32.1 ± 26.9	145.8 ± 33.8	17.6 ± 9.9	12.1 ± 6.3
2.3864	115.1 ± 21.4	35.7 ± 15.4	72.7 ± 30.7	167.3 ± 32.5	26.2 ± 8.8	43.0 ± 7.3
2.3960	441.1 ± 42.3	70.8 ± 24.3	399.2 ± 62.4	115.6 ± 33.8	133.0 ± 27.5	15.4 ± 10.7
2.6444	97.6 ± 20.1	42.8 ± 14.8	49.2 ± 22.3	65.6 ± 19.8	42.9 ± 11.4	97.0 ± 22.2
2.6464	104.0 ± 15.6	85.6 ± 21.2	100.7 ± 25.8	69.2 ± 14.2	75.6 ± 10.3	18.3 ± 12.4
2.9000	194.0 ± 24.7	35.0 ± 17.2	47.4 ± 25.4	58.5 ± 19.1	112.0 ± 13.2	32.5 ± 6.7

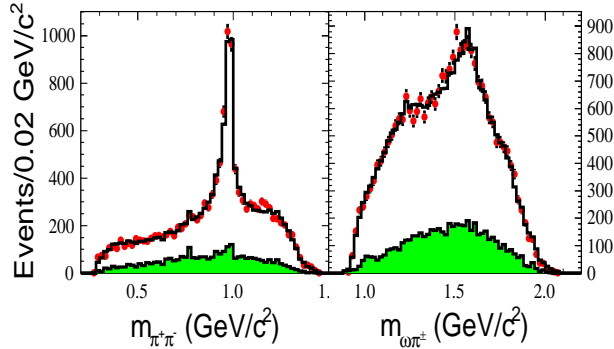


Figure 4. Projections of fit results for mass spectra $m_{\pi^+\pi^-}$ and $m_{\omega\pi^\pm}$ for group A from data sets. Dots with error bars are data, histograms are the projection of total fit results, and shaded histograms (green) are the background estimated by the ω mass sideband.

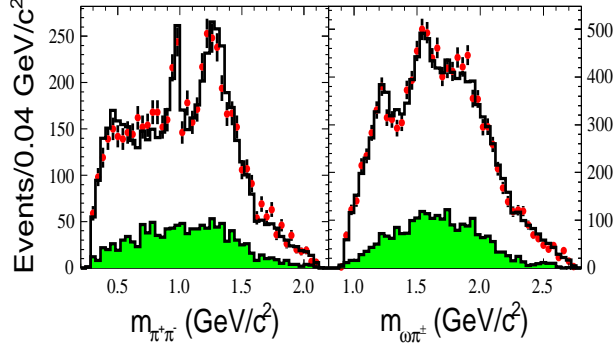


Figure 5. Projections of fit results for mass spectra $m_{\pi^+\pi^-}$ and $m_{\omega\pi^\pm}$ for group B from data sets. Dots with error bars are data, histograms are the total fit results, and shaded histograms (green) are the background estimated by the ω mass sideband.

radiative function $W(s, x)$. To unfold the Born cross section, one defines the ISR correction factor as

$$1 + \delta = \frac{\sigma_{\text{obs}}(s)}{\sigma_0(s)}, \quad (5.1)$$

with

$$\sigma_{\text{obs}}(s) = \int_{M_{\text{th}}}^{\sqrt{s}} W(s, x) \frac{\sigma_0[s(1-x)]}{|1 - \Pi(\sqrt{s})|^2} dx, \quad (5.2)$$

where $\Pi(\sqrt{s})$ is the vacuum polarization function, and we use the calculated results including the leptonic and hadronic parts both in the space-like and time-like region [72–76]. The M_{th} corresponds to the $\omega\pi^+\pi^-$ mass threshold, and x is the ratio of ISR photon energy to the beam energy.

Calculation of ISR correction factor and MC event generation are consistently done using the generator model "ConExc" [59], in which the radiative function takes the result of high-order QED calculation up to the α^2 accuracy [77], and the Born cross sections $\sigma_0(s)$ are taken as measurements by the BaBar experiment ($\sqrt{s} < 2.000$ GeV) [16] and this experiment ($\sqrt{s} > 2.000$ GeV). The shape of cross section is modeled with five Gaussian functions with parameters fixed to the fitted results, which distributes about the measured energy. To achieve the stable cross sections in this measurement, the procedure from the ISR factor calculation, MC event generation for the Born cross section calculation are iterated for several times. The iteration is stopped if the updated Born cross section reaches the accuracy within the statistical uncertainty. The ISR correction factors for each energy point are given in Table 4.

In MC event generation, the ISR photon is characterized by the soft energy and beam collinear distribution, and its angular dependence is sampled with the Bonneau and Martin formula with accuracy up to the m_e^2/s term, i.e.

$$P(\theta, x) = \frac{\sin^2 \theta - \frac{x^2 \sin^4 \theta}{2(x^2 - 2x + 2)} - \frac{m_e^2}{E^2} \frac{(1-2x) \sin^2 \theta - x^2 \cos^4 \theta}{x^2 - 2x + 2}}{\left(\sin^2 \theta + \frac{m_e^2}{E^2} \cos^2 \theta \right)^2}, \quad (5.3)$$

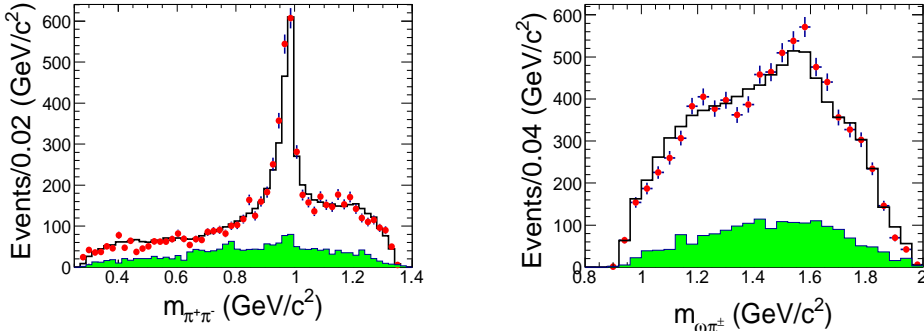


Figure 6. Comparison of $m_{\pi^+\pi^-}$ and $m_{\omega\pi^\pm}$ mass spectra between data and MC simulation at 2.1250 GeV. Dots with error bars are data, histograms are MC simulation, and shaded histograms (green) are the background estimated by the ω mass sideband.

where θ is the polar angle of the ISR photon, m_e is the electron mass and E is the beam energy. After the emission of a photon, the $\gamma^* \rightarrow \omega\pi^+\pi^-$ events are generated with the amplitude model with parameters fixed to the fitted values so that the measured intermediate states are inclusively simulated. Figure 6 shows an example of MC simulation at $\sqrt{s} = 2.125$ GeV, which yields a good agreement between data and MC simulation in the mass distribution.

5.2 Cross section for $e^+e^- \rightarrow \omega\pi^+\pi^-$

The signal yields are determined by an unbinned maximum likelihood fit to the $\pi^+\pi^-$ invariant mass distribution of ω candidate. In the fit, the signal shape is taken from the MC histogram smeared with a Gaussian function into account for the resolution difference between data and MC simulation. The background is dominated by the process $e^+e^- \rightarrow 2(\pi^+\pi^-)\pi^0$, and the corresponding shape is described by the second order Chebychev polynomial. The parameters of Gaussian function and the yields of signal and background are floated. Figure 7 shows the fitting results at the c.m. energy point of 2.125 GeV. The Born cross section is calculated from

$$\sigma^B = \frac{N_{\text{sig}} - N_{\text{mis}}}{\mathcal{L} \cdot \epsilon \cdot Br(\omega \rightarrow \pi^+\pi^-\pi^0) \cdot Br(\pi^0 \rightarrow \gamma\gamma) \cdot (1 + \delta\gamma) \cdot \frac{1}{|1-\Pi|^2}}, \quad (5.4)$$

where N_{sig} is the number of signal events obtained by fitting the $\pi^+\pi^-\pi^0$ mass distribution, N_{mis} the yields mis-combination, \mathcal{L} the integrated luminosity, ϵ is the detection efficiency obtained from weighting MC simulation according to the PWA result. The $Br(\omega \rightarrow \pi^+\pi^-\pi^0)$ and $Br(\pi^0 \rightarrow \gamma\gamma)$ are the branching fractions with values quoted from the PDG [18], $(1 + \delta\gamma)$ and $\frac{1}{|1-\Pi|^2}$ represent the correction factors for the ISR effect and vacuum polarization, respectively. To get the ISR correction factor, our measured cross sections combined with the BaBar measurements are used as the line shape input. We iterate the MC event simulation and calculation of Born cross sections for several times until the ISR factor and

Table 4. Summary of the yields of signal event (N_{sig}), number of event of mis-combination (N_{mis}), integral luminosity \mathcal{L} , radiative correction factor ($1 + \delta\gamma$), vacuum polarization factor ($\frac{1}{|1-\Pi|^2}$), detection efficiency (ϵ) and the total Born cross section of $e^+e^- \rightarrow \omega\pi^+\pi^-$ (σ^B) at various energy points \sqrt{s} , where the first uncertainties are statistical and second systematic.(see Section 6 in details.) The uncertainties of N_{sig} and N_{mis} are only statistical.

\sqrt{s} (GeV)	N_{sig}	N_{mis}	$\mathcal{L}(\text{pb}^{-1})$	$1 + \delta\gamma$	$\frac{1}{ 1-\Pi ^2}$	ϵ	$\sigma^B(\text{pb})$
2.0000	1008 \pm 37	10 \pm 3	10.1	1.1398	1.0369	0.1775	534.3 \pm 19.8 \pm 29.9
2.0500	239 \pm 18	3 \pm 2	3.4	1.1481	1.0375	0.1615	421.3 \pm 32.0 \pm 23.4
2.1000	952 \pm 37	9 \pm 3	12.2	1.1269	1.0389	0.1764	424.6 \pm 16.7 \pm 22.7
2.1250	8013 \pm 103	80 \pm 9	109.0	1.1272	1.0393	0.1704	413.6 \pm 5.4 \pm 22.3
2.1500	207 \pm 17	2 \pm 1	2.9	1.1205	1.0396	0.1587	446.4 \pm 37.4 \pm 29.1
2.1750	863 \pm 34	9 \pm 3	10.6	1.1337	1.0399	0.1646	471.0 \pm 18.8 \pm 24.6
2.2000	971 \pm 36	10 \pm 3	13.7	1.1400	1.0402	0.1631	411.5 \pm 15.4 \pm 21.4
2.2324	821 \pm 32	8 \pm 3	11.9	1.1519	1.0405	0.1556	415.6 \pm 16.4 \pm 23.0
2.3094	856 \pm 35	9 \pm 3	21.1	1.2050	1.0409	0.1503	241.6 \pm 10.0 \pm 14.4
2.3864	664 \pm 30	7 \pm 3	22.6	1.3403	1.0410	0.1470	160.8 \pm 7.3 \pm 8.4
2.3960	1943 \pm 53	19 \pm 4	66.9	1.3558	1.0410	0.1324	174.9 \pm 4.8 \pm 9.5
2.6444	624 \pm 29	6 \pm 2	33.7	1.3908	1.0394	0.1228	117.2 \pm 5.5 \pm 6.3
2.6464	606 \pm 29	6 \pm 2	34.1	1.3915	1.0394	0.1481	93.2 \pm 4.5 \pm 5.3
2.9000	999 \pm 36	10 \pm 3	106.0	1.5725	1.0328	0.1035	63.0 \pm 2.3 \pm 3.6
2.9500	136 \pm 14	2 \pm 1	16.0	1.5088	1.0289	0.1044	59.9 \pm 5.9 \pm 3.9
2.9810	130 \pm 13	2 \pm 1	16.1	1.4668	1.0246	0.1101	55.3 \pm 5.6 \pm 3.3
3.0000	119 \pm 12	1 \pm 1	15.9	1.4733	1.0207	0.1076	52.7 \pm 5.4 \pm 3.5
3.0200	134 \pm 13	2 \pm 1	17.3	1.5089	1.0145	0.1058	54.1 \pm 5.3 \pm 3.2
3.0800	543 \pm 28	5 \pm 3	126.2	1.9557	0.9149	0.0776	35.2 \pm 1.8 \pm 2.6

Born cross sections converge to their stable values. The resulting Born cross sections and related variables are summarized in Table 4.

5.3 Cross sections for the intermediate subprocesses

The Born cross sections for the intermediate subprocesses are determined with the total Born cross section of $e^+e^- \rightarrow \omega\pi^+\pi^-$ and the PWA results. Using a sample of MC truth events generated uniformly in the phase space without ISR effect, the ratio of Born cross section for a subprocess R to the total cross section is determined,

$$r_R = \frac{\sigma_R}{\sigma_{\text{tot}}}, \quad (5.5)$$

where σ_R and σ_{tot} are obtained by the partial wave amplitude weighted MC sample. The Born cross sections of intermediate subprocess at each energy point are given in Table 5, where the statistical uncertainty for the Born cross sections for an intermediate subprocess is estimated according to its signal statistical uncertainty.

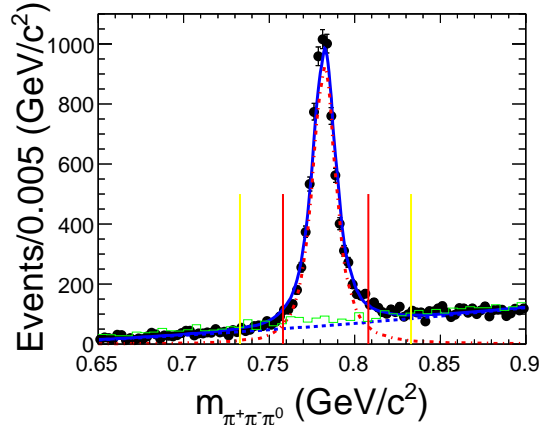


Figure 7. The $\pi^+\pi^-\pi^0$ invariant mass spectrum in the reaction $e^+e^- \rightarrow \omega\pi^+\pi^-$ (at 2.1250 GeV energy point). Dots with error bars are data, red dotted line is the signal, and the blue dashed line is the background. The blue solid line is the fit curve. The green histogram is MC simulation of the non-resonant contribution from $e^+e^- \rightarrow \pi^+\pi^-\pi^+\pi^-\pi^0$. The range between the two red vertical solid lines is regarded as signal region, and the ranges between the yellow vertical line and the red vertical line on each side of the signal peak are regarded as the sideband regions.

6 Systematic uncertainties

6.1 Uncertainties for intermediate subprocesses

Uncertainties for the measurements of intermediate subprocesses due to the partial wave analysis are from the parameterization of $f_0(500)$ and $f_0(980)$, the resonance parameters, insignificant contributions and background contamination.

- In the nominal fit, we take the $f_0(500)$ line shape as that used by the E791 Collaboration. Uncertainty associated with this parametrization is estimated by replacing it with those in Ref. [71]. The difference in the signal yield of each intermediate state is taken as systematic uncertainty.
- The parameters of $f_0(980)$ Flatté formula in the nominal fit are fixed to the measurements [70, 71]. The uncertainties are estimated by using new parameters with one

Table 5. Born cross sections for the subprocesses in unit of pb, where the first uncertainties are statistical and the second systematic.

\sqrt{s} (GeV)	$\omega f_0(500)$	$\omega f_0(980)$	$\omega f_0(1370)$
2.0000	$37.7 \pm 15.8 \pm 5.0$	$237.3 \pm 34.7 \pm 31.3$	$114.0 \pm 31.3 \pm 15.1$
2.1000	$34.7 \pm 16.2 \pm 5.5$	$117.1 \pm 20.3 \pm 18.6$	$60.3 \pm 16.9 \pm 9.6$
2.1250	$45.6 \pm 8.8 \pm 5.0$	$144.3 \pm 24.1 \pm 15.7$	$49.8 \pm 10.9 \pm 5.4$
2.1750	$91.1 \pm 23.7 \pm 6.7$	$210.1 \pm 46.9 \pm 38.5$	$90.3 \pm 41.1 \pm 16.5$
2.2000	$78.2 \pm 23.8 \pm 7.0$	$133.4 \pm 33.3 \pm 29.0$	$155.1 \pm 41.6 \pm 33.7$
2.2324	$63.8 \pm 16.0 \pm 2.5$	$154.1 \pm 34.5 \pm 30.1$	$119.2 \pm 31.9 \pm 23.3$
2.3094	$73.1 \pm 19.5 \pm 3.0$	$52.4 \pm 22.5 \pm 9.3$	$42.4 \pm 13.5 \pm 7.5$
2.3864	$34.5 \pm 8.8 \pm 5.8$	$30.7 \pm 14.3 \pm 5.2$	$21.8 \pm 10.0 \pm 3.7$
2.3960	$50.4 \pm 12.5 \pm 1.5$	$48.1 \pm 19.8 \pm 11.0$	$45.6 \pm 12.6 \pm 10.5$
2.6444	$23.1 \pm 5.4 \pm 2.2$	$10.1 \pm 3.7 \pm 1.0$	$11.6 \pm 5.4 \pm 1.1$
2.6464	$20.3 \pm 4.9 \pm 3.8$	$16.7 \pm 5.2 \pm 3.2$	$19.6 \pm 6.3 \pm 3.7$
2.9000	$15.7 \pm 2.7 \pm 1.7$	$2.8 \pm 1.4 \pm 0.3$	$3.8 \pm 2.1 \pm 0.4$
\sqrt{s} (GeV)	$\omega f_2(1270)$	$b_1^\pm(1235)\pi^\mp$	non-resonant $\omega\pi^+\pi^-$
2.0000	$107.6 \pm 21.0 \pm 14.2$	$17.9 \pm 6.0 \pm 2.4$	$1.9 \pm 0.2 \pm 0.1$
2.1000	$71.3 \pm 17.6 \pm 11.3$	$10.2 \pm 7.4 \pm 1.6$	$6.0 \pm 3.4 \pm 0.3$
2.1250	$48.0 \pm 9.4 \pm 5.3$	$19.9 \pm 4.1 \pm 2.2$	$1.6 \pm 0.1 \pm 0.1$
2.1750	$56.1 \pm 22.6 \pm 10.3$	$39.1 \pm 10.9 \pm 7.2$	$3.6 \pm 1.9 \pm 0.2$
2.2000	$90.3 \pm 27.3 \pm 19.6$	$26.8 \pm 10.7 \pm 5.8$	$6.1 \pm 4.8 \pm 0.3$
2.2324	$49.2 \pm 17.2 \pm 9.6$	$15.2 \pm 6.4 \pm 3.0$	$8.3 \pm 1.2 \pm 0.5$
2.3094	$43.4 \pm 12.6 \pm 7.7$	$6.3 \pm 3.7 \pm 1.1$	$0.8 \pm 0.4 \pm 0.1$
2.3864	$22.4 \pm 5.9 \pm 3.8$	$7.9 \pm 3.0 \pm 1.3$	$9.6 \pm 1.6 \pm 0.5$
2.3960	$13.2 \pm 4.9 \pm 3.0$	$15.2 \pm 4.7 \pm 3.5$	$0.7 \pm 0.5 \pm 0.1$
2.6444	$15.5 \pm 5.0 \pm 1.5$	$10.2 \pm 2.9 \pm 1.0$	$2.4 \pm 0.5 \pm 0.1$
2.6464	$13.5 \pm 3.8 \pm 2.6$	$14.8 \pm 3.5 \pm 2.8$	$1.9 \pm 1.3 \pm 0.1$
2.9000	$4.7 \pm 1.6 \pm 0.5$	$9.0 \pm 1.5 \pm 1.0$	$2.9 \pm 0.6 \pm 0.2$

standard deviation from the central values. The differences in the signal yields are taken as the systematic uncertainties.

- The masses and widths of intermediate states $f_0(1370)$, $f_2(1270)$, and $b_1(1235)$ are fixed to the PDG values [18] in the nominal fit. The associated uncertainties are estimated by varying masses and widths by 1σ .
- The two resonances $\rho(1450)^\pm$ and $\rho(1570)^\pm$ are partly insignificant, and not included in the baseline solution. The differences of the fits with and without including these two resonance in signal yields are assigned as systematic uncertainties.
- To estimate the uncertainty associated with the background contamination, alternative fits are performed using the number of background events changing by one

Table 6. Systematic uncertainties (in unit of %) of the $e^+e^- \rightarrow \omega\pi^+\pi^-$ cross section measurements at various energy points (\sqrt{s}). Main sources come from track efficiency (Trk), photon detection efficiency (ϵ_γ), 4C kinematic fit (4C), π^0 mass window (π^0), initial state radiative (ISR), signal shape (SS) and background shape (BS), fit range (Fit), uncertainty of luminosity measurement (\mathcal{L}), ω decay branching fraction (Br), MC statistics (Δ_{MC}) and MC model. And the total uncertainty for each point (Total) is obtained by summing the individual contributions in quadrature.

\sqrt{s} (GeV)	Trk	ϵ_γ	4C	π^0	ISR	SS	BS	Fit	\mathcal{L}	Br	Δ_{MC}	Model	Total
2.0000	4	2	1.1	1.2	1.0	1.9	0.1	0.2	1.0	0.8	0.2	1.5	5.6
2.0500	4	2	1.1	1.0	1.0	2.0	0.6	0.3	1.0	0.8	0.2	1.3	5.5
2.1000	4	2	1.2	1.2	1.0	1.4	0.1	0.5	1.0	0.8	0.2	0.7	5.3
2.1250	4	2	1.1	1.1	1.0	1.7	0.1	0.3	1.0	0.8	0.2	0.9	5.4
2.1500	4	2	1.1	2.0	1.0	3.5	0.2	0.5	1.0	0.8	0.2	1.2	6.5
2.1750	4	2	1.1	0.3	1.0	1.4	0.3	0.7	1.0	0.8	0.2	0.6	5.2
2.2000	4	2	1.0	1.1	1.0	1.0	0.4	0.1	1.0	0.8	0.2	1.0	5.2
2.2324	4	2	1.1	0.9	1.0	0.9	0.9	1.9	1.0	0.8	0.2	0.4	5.5
2.3094	4	2	1.3	1.0	1.0	1.7	0.3	2.4	1.0	0.8	0.2	0.8	6.0
2.3864	4	2	1.4	0.7	1.0	0.8	0.1	0.2	1.0	0.8	0.3	1.0	5.2
2.3960	4	2	1.2	0.2	1.0	1.8	0.9	0.9	1.0	0.8	0.3	0.3	5.4
2.6444	4	2	1.1	0.4	1.0	1.7	0.7	0.9	1.0	0.8	0.3	0.5	5.3
2.6464	4	2	1.3	0.4	1.0	1.8	1.1	1.1	1.0	0.8	0.3	1.3	5.6
2.9000	4	2	1.6	2.0	1.0	1.5	0.5	0.2	1.0	0.8	0.3	0.5	5.7
2.9500	4	2	1.5	2.0	1.0	3.5	0.4	0.6	1.0	0.8	0.3	0.5	6.5
2.9810	4	2	1.5	2.0	1.0	2.0	0.3	0.2	1.0	0.8	0.3	0.8	5.9
3.0000	4	2	1.4	3.0	1.0	3.0	0.6	0.7	1.0	0.8	0.3	0.7	6.7
3.0200	4	2	1.5	1.0	1.0	2.5	0.5	0.2	1.0	0.8	0.3	1.0	5.8
3.0800	4	2	1.3	2.0	1.0	4.5	0.8	0.6	1.0	0.8	0.4	0.9	7.2

standard deviation for various energy points. The differences in the signal yields are taken as the systematic uncertainties.

The main sources of the systematic uncertainties dominate from the $f_0(500)$ line shape, the $f_0(980)$ parameters in Flatté formula and the masses and widths of resonance states. These uncertainties are added in quadrature to give the total systematic uncertainties of intermediate states as shown in Table 5.

6.2 Uncertainties for measurements of $\sigma(e^+e^- \rightarrow \omega\pi^+\pi^-)$

The sources of systematic uncertainties associated with the cross section measurements include the tracking efficiency, photon detection, kinematic fit, π^0 mass window requirement, fitting procedure, radiative correction, luminosity measurement and branching fraction of $\omega \rightarrow \pi^+\pi^-\pi^0$.

- The uncertainty due to the tracking efficiency is estimated to be 1.0% per track [78]. Therefore 4.0% is taken as the systematic uncertainty on tracking efficiency.

- The uncertainty due to the photon detection is 1.0% per photon [79]. In this analysis, there are two photons to be required, so 2.0% is taken as a uncertainty of photon detection.
- The uncertainty associated with the kinematic fit comes from the inconsistency between the data and MC simulation of the track helix parameters. Following the procedure described in Ref. [80], the half of the difference between the efficiencies with and without the helix parameter correction is taken as the systematic uncertainty.
- The π^0 candidate is selected by requiring $|M_{\gamma\gamma} - 0.135| < 0.015 \text{ GeV}/c^2$. By changing the requirement to $|M_{\gamma\gamma} - 0.135| < 0.018 \text{ GeV}/c^2$ or $|M_{\gamma\gamma} - 0.135| < 0.013 \text{ GeV}/c^2$, the larger difference on cross section is taken as the systematic uncertainty.
- Uncertainties due to the choice of signal shape, background shape and fit range are estimated by varying the signal function from Breit-Wigner to the MC simulated shape convolved with Gaussian function, varying the background function from second-order Chebychev polynomial to third-order Chebychev polynomial and extending the fit range from (0.65, 0.89) GeV/c^2 to (0.64, 0.90) GeV/c^2 . The difference in the signal yields before and after making these changes is taken as the systematic uncertainty.
- The ISR factor is calculated with the line shape of Born cross section, which is smoothed by fitting the cross section distribution with five Gaussian functions. MC samples with ISR effect are generated according to the input line shape. Using the renewed MC samples, we re-estimate the efficiency and ISR correction factor and update the cross section. The iterations are done until the results are stable. Finally, the difference between the last two iterations are considered as the iteration uncertainty from ISR correction, their values are less than 1.0%. To be conservative, 1.0% is taken as the corresponding systematic uncertainty for all the energy points.
- The integrated luminosities of these data samples are measured using large angle Bhabha events, and uncertainties of $\sim 1.0\%$ [81] are propagated to the cross section measurements. The uncertainty in $Br(\omega \rightarrow \pi^+\pi^-\pi^0)$ is quoted as 0.8% from PDG [18].
- The uncertainty from MC statistics is estimated by the number of generated events, calculated by $\Delta_{MC} = \sqrt{(1 - \epsilon)/\epsilon}/\sqrt{N}$, where $N = 1000000$ is the number of generated events at each energy point.
- The uncertainty due to the MC simulation modeled by amplitude analysis was investigated by smearing masses and widths of intermediate states event by event within 1σ assuming they follow Gaussian distribution. The difference in detection efficiency between with and without smearing is taken as the systematic uncertainty, which is about 1%. The effect due to insignificant intermediate states, such as $\rho(1450)$, and $\rho(1570)$ is investigated by adding them to the nominal fit. The difference in MC detection efficiency with and without these two states is also taken as the systematic uncertainty, which is varying from 0.2% to 1% dependent on the energy point.

The total uncertainty due to the MC model on amplitude analysis is sum of these uncertainties in quadrature.

The systematic uncertainties for all energy points are listed in Table 6. These systematic uncertainties are assumed to be independent and summed in quadrature.

7 Fit to the line shapes

7.1 Line shape of $e^+e^- \rightarrow \omega\pi^+\pi^-$

The measured Born cross sections are shown in Fig. 8, where a clear structure is observed around 2.25 GeV. A minimized χ^2 fit incorporating the correlated and uncorrelated uncertainties is performed to the measured cross section with the function:

$$\sigma^B(\sqrt{s}) = |\sigma_r(\sqrt{s})e^{i\phi} + \sigma_c(\sqrt{s})|^2, \quad (7.1)$$

where ϕ is the phase of the resonance structure relative to the continuum components, and σ_r and σ_c are the cross sections for the resonance and continuum components, respectively. They are taken as

$$\sigma_r(\sqrt{s}) = \frac{m_r}{\sqrt{s}} \frac{\sqrt{12\pi C \Gamma_r^{ee} Br \Gamma_r}}{s - m_r^2 + im_r \Gamma_r} \sqrt{\frac{P(\sqrt{s})}{P(m_r)}} \quad (7.2)$$

$$\sigma_c(\sqrt{s}) = \frac{a\sqrt{P(\sqrt{s})}}{\sqrt{s}^b} \quad (7.3)$$

where $\sigma_r(\sqrt{s})$ stands for the resonant component [82], in which m_r and Γ_r are the mass and width of the resonant structure near 2.25 GeV. The parameter $\Gamma_r^{ee} \cdot Br$ is the product of partial width of the resonance decaying to the e^+e^- and the branching fraction to the $\omega\pi^+\pi^-$ final state. The continuum part $\sigma_c(\sqrt{s})$ is parameterized by parameters a and b . All the six parameters in the fit are floated, where the function $P(\sqrt{s})$ is calculated three-body phase space factor and C is a conversion constant which equals to 3.893×10^5 nb GeV² [16]. For the two-body decay, it is taken as p/\sqrt{s} , where p is the magnitude of the momentum for one of the two particles. For the three-body decay to the $\pi^+\pi^-\omega$ final state, one has

$$P(s) = \frac{1}{4s} \int_{2m_\pi}^{\sqrt{s}-m_\omega} \sqrt{(m_{\pi^+\pi^-}^2 - 4m_\pi^2)[s - (m_{\pi^+\pi^-} + m_\omega)^2][s - (m_{\pi^+\pi^-} - m_\omega)^2]} dm_{\pi^+\pi^-}, \quad (7.4)$$

where m_ω and $m_{\pi^+\pi^-}$ are the mass of ω particle and the invariant mass of $\pi^+\pi^-$, respectively. The results of the fit to the measured cross section are shown in Fig. 8. The fit has two solutions with equally good fit quality and identical masses and widths of the resonances, while the phases and the products of the electronic widths with the branching fractions are different. We observe the structure around 2.25 GeV with statistical significance of 10.3σ which is determined from the change in the χ^2 value with and without it in the fit versus the change of the number of degrees of freedom. The best fit gives a fit quality of $\chi^2/\text{n.d.f} = 20.6/13$. The fit parameters of two solutions are listed in Table 7. Due

to the interference effect, the fitted parameter b is $b = 4.4 \pm 0.1$ in both two solutions. It is interesting to note that this is different from the single virtual photon contribution with $b = 1$. The obtained mass here is consistent with that of simultaneous fit above within 2 times standard deviations.

Table 7. Resonance parameters obtained in the fit to the $e^+e^- \rightarrow \omega\pi^+\pi^-$ cross section. The uncertainties are statistical only.

Parameter	Solution I	Solution II
m_r (MeV/ c^2)	2250 ± 25	2250 ± 25
Γ_r (MeV)	125 ± 43	125 ± 43
$\Gamma_r^{ee} \cdot Br$ (eV)	0.9 ± 0.4	52.9 ± 17.0
ϕ (rad.)	2.4 ± 0.3	-1.8 ± 0.1
$a(10^3)(\text{pb}^{1/2})$	1.1 ± 0.2	1.1 ± 0.2
b	4.4 ± 0.1	4.4 ± 0.1
Significance	10.3σ	

To estimate the systematic uncertainties for the resonant parameters, an alternative fit is performed by parameterizing the continuum component with an exponential function[83] to determine the uncertainties associated with the continuum component :

$$\sigma_c(\sqrt{s}) = \sqrt{P(\sqrt{s})e^{p_0u}p_1}, \quad (7.5)$$

where p_0 and p_1 are float parameters and $u = \sqrt{s} - (2m_\pi^{PDG} + m_\omega)$. The differences of the results between the alternative fit and the nominal fit are taken as systematic uncertainties for resonant parameters. The systematic uncertainties associated with the signal model are also studied by using a relativistic Breit-Wigner function with energy-dependent width as signal shape. Their differences are found to be negligible. Eventually, the mass and width of the resonance are determined to be $m_r = 2250 \pm 25 \pm 27$ MeV/ c^2 and $\Gamma_r = 125 \pm 43 \pm 15$ MeV with a statistical significance of 10.3σ . In addition, the $\Gamma_r^{ee} \cdot Br$ is determined to $0.9 \pm 0.4 \pm 0.4$ eV or $52.9 \pm 17.0 \pm 13.1$ eV for two solutions from the fit, where the first uncertainties are statistical and the second ones are systematic.

7.2 Cross section of $e^+e^- \rightarrow \omega\pi\pi$

Cross sections of $e^+e^- \rightarrow \omega\pi\pi$ are summation of measurements for $e^+e^- \rightarrow \omega\pi^0\pi^0$ [50] and $e^+e^- \rightarrow \omega\pi^+\pi^-$. Cross sections for $\omega\pi\pi$ are consistent with that for $\omega\pi^0\pi^0$ within 2σ uncertainties. This indicates that the pion production in the $\omega\pi\pi$ decay comply with the SU(3)-flavor symmetry. The summed cross sections at various energy points are listed in Table 8, where the first uncertainties are statistical, and the second ones are systematic. We fit the $e^+e^- \rightarrow \omega\pi\pi$ cross sections with the same method as Section 7.1 (see Fig. 9). The resultant parameters are obtained and tabulated in Table 9. After considering the systematic uncertainty, the mass and width of resonance near 2.25 GeV are $2232 \pm 19 \pm 27$

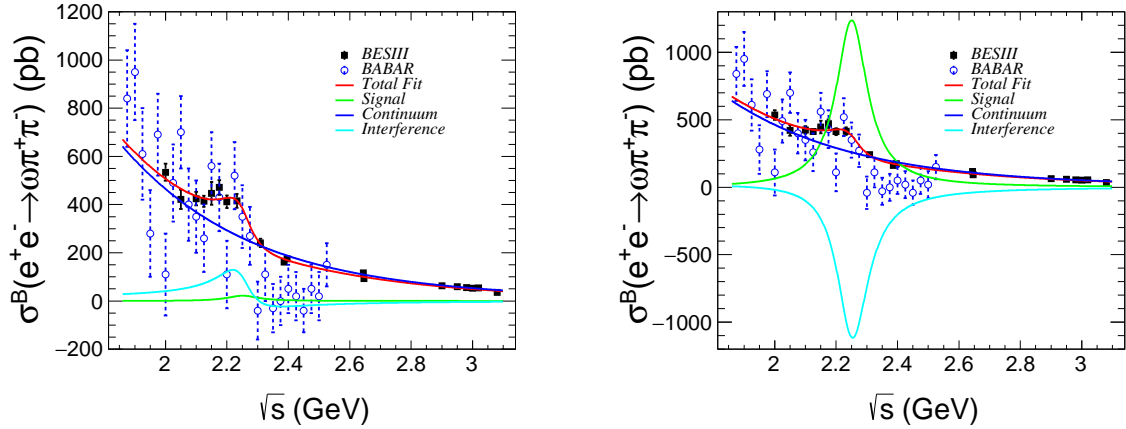


Figure 8. Fits to the measured $e^+e^- \rightarrow \omega\pi^+\pi^-$ cross sections. The dots with error bars are the measured Born cross sections at c.m. energies between 2.000 GeV and 3.080 GeV (BESIII data), where the error bars include both statistical and systematic uncertainties. Circles with error bars (hatched line) are the results of the BaBar experiment. The red solid curve is the total fit result. The blue solid curve represents continuum component, the green curve stands for resonant component and the cyan line is the interference of the two components. The two plots are the results of Solution I (left) and Solution II (right), respectively.

MeV/ c^2 and $91 \pm 53 \pm 20$ MeV, respectively. The values of $\Gamma_r^{ee} \cdot Br$ for the resonance decay are $0.9 \pm 0.5 \pm 0.2$ eV and $61.1 \pm 32.1 \pm 15.4$ eV for the two solutions. The statistical significance of the structure is 7.6σ .

Table 8. The cross sections of $e^+e^- \rightarrow \omega\pi\pi$, where the first uncertainties are statistical, the second systematic.

\sqrt{s} (GeV)	cross section(pb)	\sqrt{s}	cross section(pb)
2.000	$828.2 \pm 28.1 \pm 58.0$	2.396	$252.2 \pm 6.2 \pm 13.6$
2.050	$700.1 \pm 46.0 \pm 49.5$	2.644	$176.3 \pm 7.2 \pm 9.4$
2.100	$645.2 \pm 23.1 \pm 39.0$	2.646	$149.0 \pm 6.4 \pm 8.2$
2.125	$627.3 \pm 7.6 \pm 45.7$	2.900	$88.60 \pm 2.8 \pm 5.0$
2.150	$654.6 \pm 49.0 \pm 50.9$	2.950	$80.40 \pm 7.2 \pm 5.2$
2.175	$694.8 \pm 24.8 \pm 49.7$	2.981	$85.70 \pm 7.4 \pm 4.9$
2.200	$645.8 \pm 21.4 \pm 40.2$	3.000	$68.60 \pm 6.5 \pm 4.5$
2.232	$600.7 \pm 21.3 \pm 46.1$	3.020	$70.00 \pm 6.2 \pm 4.0$
2.309	$343.1 \pm 12.9 \pm 25.2$	3.080	$48.10 \pm 2.2 \pm 3.4$
2.386	$249.1 \pm 10.3 \pm 12.7$		

We also compute the contribution of our cross section measurement $\sigma^{\text{born}}(e^+e^- \rightarrow \omega\pi\pi)$

Table 9. Resonance parameters obtained in the fit to the $e^+e^- \rightarrow \omega\pi\pi$ cross section. The uncertainties are statistical only.

Parameter	Solution I	Solution II
m_r (MeV/c ²)	2232 ± 19	2232 ± 19
Γ_r (MeV)	93 ± 53	93 ± 53
$\Gamma_r^{ee} \cdot Br$ (eV)	0.9 ± 0.5	61.1 ± 32.1
ϕ (rad)	2.4 ± 0.3	-1.7 ± 0.1
$a(10^3)(\text{pb}^{1/2})$	1.7 ± 0.2	1.7 ± 0.2
b	4.6 ± 0.1	4.6 ± 0.1
Significance	7.6 σ	

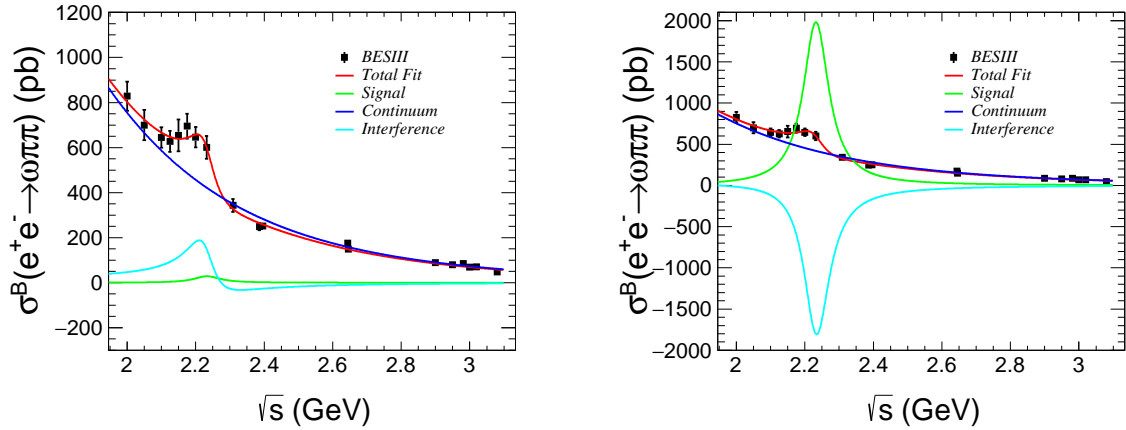


Figure 9. Fits to the cross sections of $e^+e^- \rightarrow \omega\pi\pi$. The dots with error bars are the measured Born cross sections at c.m. energies between 2.000 GeV and 3.080 GeV (BESIII data), where the error bars include both statistical and systematic uncertainties. The red solid curves are the total fit results. The blue solid curves represent continuum components, the green curves stand for resonant components and the cyan line are the interference of the two components. The two plots are the results of Solution I (left) and Solution II (right), respectively.

to the hadronic contribution of $(g-2)_\mu$,

$$a_\mu^{\omega\pi\pi}(2.00-3.08\text{GeV}) = \frac{1}{4\pi^3} \int_{(2.00\text{GeV})^2}^{(3.08\text{GeV})^2} ds' K(s') \sigma_{\omega\pi\pi}^{\text{born}}, \quad (7.6)$$

where $K(s')$ is the kernel function [84]. Our result, $a_\mu^{\omega\pi\pi}(2.00-3.08\text{GeV}) = (0.104 \pm 0.005 \pm 0.007) \times 10^{-10}$ is found to be the first measurement for the $e^+e^- \rightarrow \omega\pi\pi$ decay.

7.3 The $X(2230)$ decays via intermediate states

Using the measured cross sections via the intermediate states as tabulated in Table 5, we perform a simultaneous fit to the $X(2230)$ decays of cross sections σ_i^{exp} with $i = 1, 2, \dots, 5$

for the mode $\omega f_0(500)$, $\omega f_0(980)$, $\omega f_0(1370)$, $\omega f_2(1270)$, and $b_1(1235)\pi$, respectively. At the energy point \sqrt{s} , the cross section for mode f is described by $\sigma_f^{\text{fit}}(\sqrt{s}) = |\sigma_r e^{i\phi}(\sqrt{s}, f) + \sigma_c(\sqrt{s}, f)|^2$, where σ_r and σ_c is given by Eq. (7.2 and 7.3), except that the phase space factor is replaced by that of the two-body decay. Taking into consideration of the error correlations among these five modes, the χ^2 function is minimized, which is defined by

$$\chi^2 = \sum_s \Sigma^T V^{-1} \Sigma, \text{ with} \\ \Sigma^T = (\sigma_1^{\text{exp}} - \sigma_1^{\text{fit}}, \sigma_2^{\text{exp}} - \sigma_2^{\text{fit}}, \sigma_3^{\text{exp}} - \sigma_3^{\text{fit}}, \sigma_4^{\text{exp}} - \sigma_4^{\text{fit}}, \sigma_5^{\text{exp}} - \sigma_5^{\text{fit}}), \quad (7.7)$$

where V is a covariance matrix with element $V_{ij} = \rho_{ij}\sigma_i\sigma_j$, and ρ_{ij} is a correlation coefficient, and determined by the errors of interference between mode i and j . We take $\rho_{ij} = 1$ if $i = j$. The sum over s runs over all energy points involved in the fit. The symbols σ_i^{exp} and σ_i^{fit} indicate the measured and the predicted cross section of i -th bin in the fit, respectively.

Figure 10 shows results of simultaneous fit to these five decay modes. In the fit, the $X(2230)$ is assumed as a vector meson, and its mass and width are $2200 \pm 11 \pm 17$ MeV/ c^2 and $74 \pm 20 \pm 24$ MeV, respectively. Here the systematic uncertainties of mass and width are determined by the same method as above section 7.1. The significance is about 7.9σ . The resultant values of $\Gamma_r^{ee} \cdot Br$ are tabulated in Table 10, where Γ_r^{ee} is the partial width of the $X(2230)$ decaying to e^+e^- , and Br is the branching fraction for the $X(2230)$ decaying to final state $\omega\pi\pi$ via intermediate state f . Two solutions are found with equally good fit quality. No structure around 2.25 GeV is seen in the phase space decay as shown in Fig. 10 (f), which indicates that the vector meson favors the intermediate decay.

Table 10. The $\Gamma_r^{ee} \cdot Br$ values with simultaneous fit to the cross sections for the five decay modes, where the uncertainties are statistical only.

	Solution I	Solution II
$e^+e^- \rightarrow f$	$\Gamma_r^{ee} \cdot Br$ (eV)	$\Gamma_r^{ee} \cdot Br$ (eV)
$\omega f_0(500)$	2.9 ± 2.5	1.2 ± 0.5
$\omega f_0(980)$	5.9 ± 5.0	3.2 ± 1.0
$\omega f_0(1370)$	6.4 ± 5.4	3.1 ± 1.0
$\omega f_2(1270)$	2.5 ± 2.1	1.1 ± 0.6
$b_1(1235)\pi$	1.1 ± 1.0	0.2 ± 0.2

8 Conclusion and discussion

In summary, the Born cross sections of $e^+e^- \rightarrow \omega\pi^+\pi^-$ are measured using 647 pb $^{-1}$ data samples collected with the BESIII detector at nineteen c.m. energies from 2.000 GeV to 3.080 GeV. The measured cross sections are compared with previous result from the BaBar experiment [16] with precision improved by a factor of 3. The resonance structure near 2.25 GeV is observed significantly in this analysis, and confirms the observation in the previous analysis $e^+e^- \rightarrow \omega\pi^0\pi^0$ [50]. The energy dependence of the total cross section for

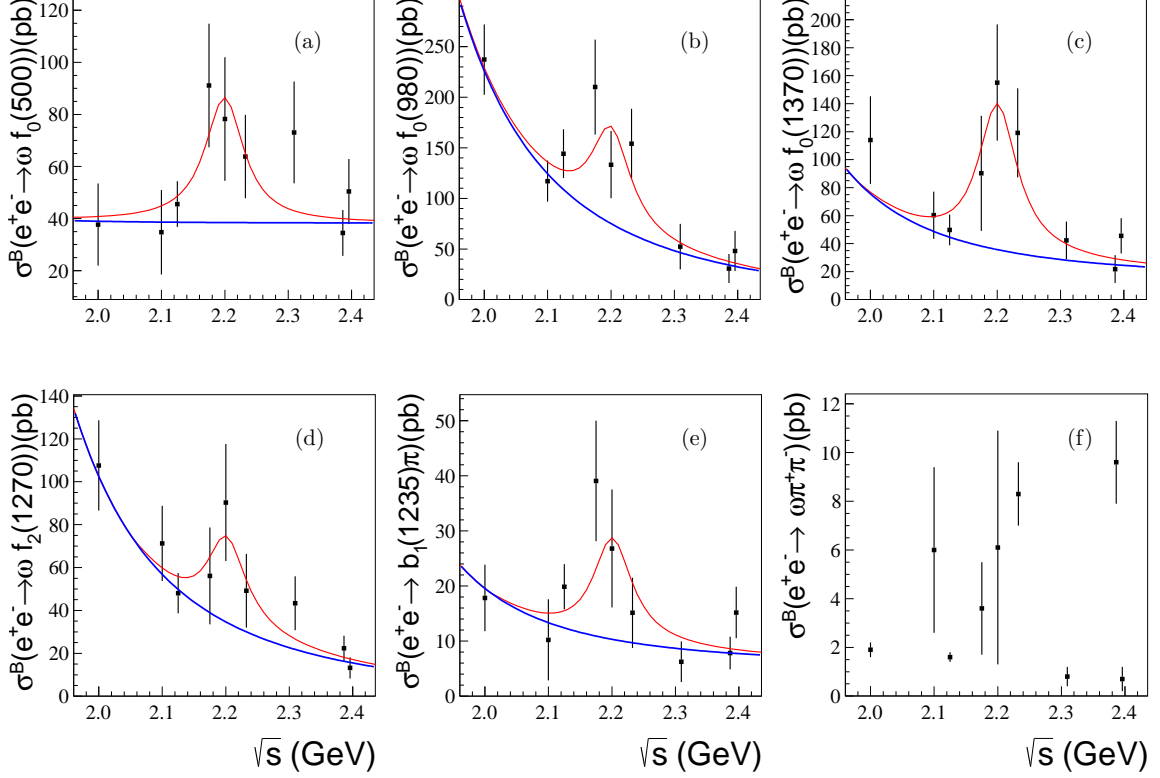


Figure 10. Cross sections via intermediate states for the $\omega f_0(500)$ (a), $\omega f_0(980)$ (b), $\omega f_0(1370)$ (c), $\omega f_2(1270)$ (d), $b_1(1235)\pi$ (e) processes. Points with error bars are the measured cross sections, the curves are the total fit results (red line), and the blue line means the continuum parts. The bottom right plot (f) displays the contribution from phase space decay $e^+e^- \rightarrow \omega\pi^+\pi^-$.

$e^+e^- \rightarrow \omega\pi^+\pi^-$ and $\omega\pi^0\pi^0$ in the energy region of interest is shown in Fig. 9. It is fitted by a coherent sum of resonant and nonresonant contributions. From the fit to the $e^+e^- \rightarrow \omega\pi\pi$ cross sections, we obtain the mass and width of this structure to be $2232 \pm 19 \pm 27 \text{ MeV}/c^2$ and $93 \pm 53 \pm 20 \text{ MeV}$, respectively. The fit values of $\Gamma_r^{ee} \cdot Br$ are $0.9 \pm 0.5 \pm 0.2 \text{ eV}$ or $61.1 \pm 32.1 \pm 15.4 \text{ eV}$ dependent on the interference pattern. The structure near 2.25 GeV seen by the BaBar experiment [17] are confirmed by this work within one standard deviation. We also perform the amplitude analysis on decays via the intermediate states, such as $e^+e^- \rightarrow \omega f_0(500)$, $\omega f_0(980)$, $\omega f_0(1370)$, $\omega f_2(1270)$ and $b_1(1235)\pi$. The line shapes of Born cross sections are shown in Fig. 10. Cross sections of intermediate subprocesses with high accuracy will help to examine properties and better reveal the nature of the resonance. As for the exclusive process of $e^+e^- \rightarrow \omega\pi\pi$, we computed its cross section of the hadronic contribution to $(g-2)_\mu$, and found the contribution is small in the energy region between 2.000 GeV and 3.080 GeV.

9 Acknowledgments

The BESIII collaboration thanks the staff of BEPCII and the IHEP computing center for their strong support. This work is supported in part by National Key Research and Development Program of China under Contracts Nos. 2020YFA0406400, 2020YFA0406300, National Natural Science Foundation of China (NSFC) under Contracts Nos. 11875262, 12175244, 11835012, 11625523, 11635010, 11735014, 11822506, 11835012, 11935015, 11935016, 11935018, 11625523, 11605196, 11605198, 11705192, 12035013, 11961141012, 11950410506, 12061131003; the Chinese Academy of Sciences (CAS) Large-Scale Scientific Facility Program; Joint Large-Scale Scientific Facility Funds of the NSFC and CAS under Contracts Nos. U2032110, U1732263, U1832207, U1832103, U2032111; CAS Key Research Program of Frontier Sciences under Contracts Nos. QYZDJ-SSW-SLH003, QYZDJ-SSW-SLH040; 100 Talents Program of CAS; INPAC and Shanghai Key Laboratory for Particle Physics and Cosmology; ERC under Contract No. 758462; German Research Foundation DFG under Contracts Nos. 443159800, Collaborative Research Center CRC 1044, FOR 2359, FOR 2359, GRK 214; Istituto Nazionale di Fisica Nucleare, Italy; Ministry of Development of Turkey under Contract No. DPT2006K-120470; National Science and Technology fund; Olle Engkvist Foundation under Contract No. 200-0605; STFC (United Kingdom); The Knut and Alice Wallenberg Foundation (Sweden) under Contract No. 2016.0157; The Royal Society, UK under Contracts Nos. DH140054, DH160214; The Swedish Research Council; U. S. Department of Energy under Contracts Nos. DE-FG02-05ER41374, DE-SC-0012069.

References

- [1] BESIII Collaboration, *Observation of a charged charmoniumlike structure in $e^+e^- \rightarrow \pi^+\pi^- J/\psi$ at $\sqrt{s}=4.26$ GeV*, *Phys. Rev. Lett.* **110** (2013) 252001.
- [2] BESIII Collaboration, *Observation of a charged charmoniumlike structure $Z_c(4020)$ and search for the $Z_c(3900)$ in $e^+e^- \rightarrow \pi^+\pi^- h_c$* , *Phys. Rev. Lett.* **111** (2013) 242001.
- [3] BESIII Collaboration, *Observation of a charged $(D\bar{D}^*)^\pm$ mass peak in $e^+e^- \rightarrow \pi D\bar{D}^*$* , *Phys. Rev. Lett.* **112** (2014) 022001.
- [4] BESIII Collaboration, *Observation of a charged charmoniumlike structure in $e^+e^- \rightarrow (D^*\bar{D}^*)^\pm\pi^\mp$ at $\sqrt{s}=4.26$ GeV*, *Phys. Rev. Lett.* **112** (2014) 132001.
- [5] BESIII Collaboration, *Observation of $e^+e^- \rightarrow \pi^0\pi^0 h_c$ and a neutral charmoniumlike structure $Z_c(4020)^0$* , *Phys. Rev. Lett.* **113** (2014) 212002.
- [6] BESIII Collaboration, *Observation of $Z_c(3900)^0$ in $e^+e^- \rightarrow \pi^0\pi^0 J/\psi$* , *Phys. Rev. Lett.* **115** (2015) 112003.
- [7] BESIII Collaboration, *Observation of a neutral charmoniumlike state $Z_c(4025)^0$ in $e^+e^- \rightarrow (D^*\bar{D}^*)^0\pi^0$* , *Phys. Rev. Lett.* **115** (2015) 182002.
- [8] BESIII Collaboration, *Observation of a neutral structure near the $D\bar{D}^*$ mass threshold in $e^+e^- \rightarrow (D\bar{D}^*)^0\pi^0$ at $\sqrt{s} = 4.226$ and 4.257 GeV*, *Phys. Rev. Lett.* **115** (2015) 222002.
- [9] Belle Collaboration, *Study of $e^+e^- \rightarrow \pi^+\pi^- J/\psi$ and observation of a charged charmoniumlike state at Belle*, *Phys. Rev. Lett.* **110** (2013) 252002.

- [10] T. Xiao, S. Dobbs, A. Tomaradze and K. K. Seth, *Observation of the charged hadron $Z_c^\pm(3900)$ and evidence for the neutral $Z_c^0(3900)$ in $e^+e^- \rightarrow \pi\pi J/\psi$ at $\sqrt{s}=4170$ MeV*, [Phys. Lett. B **727** \(2013\) 366](#).
- [11] BESIII Collaboration, *Observation of a near threshold structure in the K^+ recoil mass spectrum in $e^+e^- \rightarrow K^+(D_s^- D^{*0} + D_s^{*-} D^0)$* , [Phys. Rev. Lett. **126** \(2021\) 102001](#).
- [12] BESIII Collaboration, *Evidence for a neutral near-threshold structure in the K_S^0 recoil-mass spectra in $e^+e^- \rightarrow K_S^0 D_s^+ D^{*-}$ and $e^+e^- \rightarrow K_S^0 D_s^{*+} D^-$* , [arXiv:2204.13703v3](#).
- [13] Muon g-2 Collaboration, *Measurement of the positive muon anomalous magnetic moment to 0.46 ppm*, [Phys. Rev. Lett. **126** \(2021\) 141801](#).
- [14] M. Davier, *The hadronic contribution to $(g-2)(\mu)$* , [Nucl. Phys. B, Proc. Suppl. **169** \(2007\) 288](#).
- [15] T. Aoyama, N. Asmussen, M. Benayoun *et al.* *The anomalous magnetic moment of the muon in the Standard model*, [Phys. Rept. **887** \(2020\) 1](#).
- [16] BaBar Collaboration, *The $e^+e^- \rightarrow 2(\pi^+\pi^-)\pi^0$, $2(\pi^+\pi^-)\eta$, $K^+K^-\pi^+\pi^-\pi^0$ and $K^+K^-\pi^+\pi^-\eta$ cross section measured with initial-state radiation*, [Phys. Rev. D **76** \(2007\) 092005](#).
- [17] BaBar Collaboration, *Resonance in e^+e^- annihilation near 2.2 GeV*, [Phys. Rev. D **101** \(2020\) 012011](#).
- [18] Particle Data Group, *Review of particle physics*, [Prog. Theor. Exp. Phys. **2020** \(2020\) 083C01](#).
- [19] G. J. Ding and M. L. Yan, *$Y(2175)$: Distinguish hybrid state from higher quarkonium*, [Phys. Lett. B **657** \(2007\) 49](#).
- [20] X. Wang *et al.*, *Non-strange partner of strangeonium-like state $Y(2175)$* , [Phys. Rev. D **85** \(2012\) 074024](#).
- [21] S. S. Afonin and I. V. Posenkov, *Universal description of radially excited heavy and light vector mesons*, [Phys. Rev. D **90** \(2014\) 094020](#).
- [22] C. Q. Pang, *Excited states of ϕ meson*, [Phys. Rev. D **99** \(2019\) 074015](#).
- [23] C. G. Zhao *et al.*, *$\phi(2170)$ production in the process $\gamma P \rightarrow \eta\phi p$* , [Phys. Rev. D **99** \(2019\) 114014](#).
- [24] Q. Li *et al.*, *Mass spectrum and strong decays of strangeonium in a constituent quark model* [Chin. Phys. C **45** \(2021\) 023116](#).
- [25] G. J. Ding and M. L. Yan, *A candidate for 1^{--} strangeonium hybrid*, [Phys. Lett. B **650** \(2007\) 390](#).
- [26] J. Ho, R. Berg *et al.*, *Is the $Y(2175)$ a strangeonium hybrid meson*, [Phys. Rev. D **100** \(2019\) 034012](#).
- [27] Z. G. Wang, *Analysis of the $Y(2175)$ as a tetraquark state with QCD sum rules*, [Nucl. Phys. A **791** \(2007\) 106](#).
- [28] H. X. Chen *et al.*, *$Y(2175)$ state in the QCD sum rule*, [Phys. Rev. D **78** \(2008\) 034012](#).
- [29] N. V. Drenska *et al.*, *Higher tetraquark particles*, [Phys. Lett. B **669** \(2008\) 160](#).
- [30] C. R. Deng *et al.*, *Tetraquark state and multibody interaction*, [Phys. Rev. D **82** \(2010\) 074001](#).

- [31] H. W. Ke and X. Q. Li, *Study of the strong decays of $\phi(2170)$ and the future charm-tau factory*, [Phys. Rev. D **99** \(2019\) 036014](#).
- [32] S. S. Agaev *et al.*, *Nature of the vector resonance $Y(2175)$* , [Phys. Rev. D **101** \(2020\) 074012](#).
- [33] R. R. Dong *et al.*, *QCD sum rule studies on the $ss\bar{s}\bar{s}$ tetraquark states of $J^{PC} = 0^{-+}$* , [Eur. Phys. J. C **80** \(2020\) 749](#).
- [34] F. X. Liu *et al.*, *Fully-strange tetraquark $ss\bar{s}\bar{s}$ spectrum and possible experimental evidence*, [Phys. Rev. D **103** \(2021\) 016016](#).
- [35] E. Klempt and A. Zaitsev, *Glueballs hybrids multiquark experimental facts versus QCD inspired concepts*, [Phys. Rep. **454** \(2007\) 1](#).
- [36] L. Zhao *et al.*, *Meson-exchange model for the $\Lambda\bar{\Lambda}$ interaction*, [Phys. Rev. D **87** \(2013\) 054034](#).
- [37] C. Deng *et al.*, *Baryonia and near-threshold enhancements*, [Phys. Rev. D **88** \(2013\) 074007](#).
- [38] Y. B. Dong *et al.*, *Selected strong decays of $\eta(2225)$ and $\phi(2170)$ as $\Lambda\bar{\Lambda}$ bound states*, [Phys. Rev. D **96** \(2017\) 074027](#).
- [39] Y. L. Yang *et al.*, *Electromagnetic form factors of Λ hyperon in the vector meson dominance model*, [Phys. Rev. D **100** \(2019\) 073007](#).
- [40] A. Martinez Torres *et al.*, *$X(2175)$ as a resonant state of the ϕK anti- K system*, [Phys. Rev. D **78** \(2008\) 074031](#).
- [41] S. Gomez-Avila *et al.*, *$\phi K^+ K^-$ production in electron-positron annihilation*, [Phys. Rev. D **79** \(2009\) 034018](#).
- [42] BESIII Collaboration, *Measurement of $e^+e^- \rightarrow K^+K^-$ cross section at $\sqrt{s} = 2.00 - 3.08$ GeV*, [Phys. Rev. D **99** \(2019\) 032001](#).
- [43] BESIII Collaboration, *Observation of a resonant structure in $e^+e^- \rightarrow K^+K^-\pi^0\pi^0$* , [Phys. Rev. Lett. **124** \(2020\) 112001](#).
- [44] BESIII Collaboration, *Observation of a structure in $e^+e^- \rightarrow \phi\eta'$* , [Phys. Rev. D **102** \(2020\) 012008](#).
- [45] BESIII Collaboration, *Observation of a resonant structure in $e^+e^- \rightarrow \omega\eta$ and another in $e^+e^- \rightarrow \omega\pi^0$ at center-of-mass energies between 2.00 and 3.08 GeV*, [Phys. Lett. B **813** \(2021\) 136059](#).
- [46] BESIII Collaboration, *Cross section measurement of $e^+e^- \rightarrow K_S^0 K_L^0$ at $\sqrt{s} = 2.00 - 3.08$ GeV*, [Phys. Rev. D **104** \(2021\) 092014](#).
- [47] BESIII Collaboration, *Measurement of the Born cross sections for $e^+e^- \rightarrow \eta'\pi^+\pi^-$ at center-of-mass energies between 2.00 and 3.08 GeV*, [Phys. Rev. D **103** \(2021\) 072007](#).
- [48] BESIII Collaboration, *Cross section measurement of $e^+e^- \rightarrow K+K^-K^+K^-$ and ϕK^+K^- at center-of-mass energies from 2.10 to 3.08 GeV*, [Phys. Rev. D **100** \(2019\) 032009](#).
- [49] C. Q. Pang *et al.*, *Study of the ω meson family and newly observed ω -like state $X(2240)$* , [Phys. Rev. D **101** \(2020\) 074022](#).
- [50] BESIII Collaboration, *Measurement of the $e^+e^- \rightarrow \omega\pi^0\pi^0$ cross section at center-of-mass energies from 2.00 to 3.08 GeV*, [Phys. Rev. D **105** \(2022\) 032005](#).
- [51] BESIII Collaboration, *Design and construction of the BESIII detector*, [Nucl. Instrum. Meth. A **614** \(2010\) 345](#).

- [52] C. H. Yu *et al.*, *BEPCII performance and beam dynamics studies on luminosity*, [Proceedings of IPAC2016, Busan, Korea, 2016, doi:10.18429/JACoW-IPAC2016-TUYA01](#).
- [53] BESIII Collaboration, *Luminosities and energies of e^+e^- collision data taken between $\sqrt{s}=4.612$ GeV and 4.946 GeV at BESIII*, [hep-ex:2205.04809](#)
- [54] BESIII Collaboration, *Future physics programme of BESIII*, [Chin. Phys. C **44** \(2020\) 040001](#).
- [55] GEANT4 Collaboration, *GEANT4-a simulation toolkit*, [Nucl. Instrum. Methods Phys. Res. Sect. A **506** \(2003\) 250](#).
- [56] Francisco Campanario *et al.*, *Standard model radiative corrections in the pion form factor measurements do not explain the a_μ anomaly*, [Phys. Rev. D **100** \(2019\) 076004](#).
- [57] H. Czyz, J. H. Kuhn and S. Tracz, *et al.*, *Nucleon form factors and final state radiative corrections to $e^+e^- \rightarrow \bar{p}p\gamma^*$* , [Phys. Rev. D **90** \(2014\) 114021](#).
- [58] R. G. Ping *et al.*, *Tuning and validation of hadronic event generator for R value measurements in the tau-charm region*, [Chin. Phys. C **40** \(2016\) 113002](#).
- [59] R. G. Ping *et al.*, *An exclusive event generator for e^+e^- scan experiments*, [Chin. Phys. C **38** \(2014\) 083001](#).
- [60] B. Andersson and H. M. Hu, *Few-body states in lund string fragmentation model*, [arXiv:hep-ph/9910285](#).
- [61] X. Y. Zhou *et al.*, *A generic tool for the event type analysis of inclusive Monte Carlo samples in high energy physics experiments*, [Comput. Phys. Comm. **258** \(2021\) 107540](#).
- [62] LHCb Collaboration, *Observation of $J/\psi p$ resonances consistent with pentaquark states in $\Lambda_b^0 \rightarrow J/\psi K^- p$ decays*, [Phys. Rev. Lett. **115** \(2015\) 072001](#).
- [63] Belle Collaboration, *Experimental constraints on the spin and parity of the $Z(4430)^+$* , [Phys. Rev. D **88** \(2013\) 074026](#).
- [64] H. Chen and R. G. Ping, *Coherent helicity amplitude for sequential decays*, [Phys. Rev. D **95** \(2017\) 076010](#).
- [65] S. M. Berman and M. Jacob, *Spin and parity analysis in two-step decay processes*, [Phys. Rev. B **139**, \(1965\) 1608](#).
- [66] S. U. Chung, *General formulation of covariant helicity coupling amplitudes*, [Phys. Rev. D **57** \(1998\) 431](#).
- [67] S. U. Chung, *Helicity coupling amplitude in tensor formalism*, [Phys. Rev. D **48** \(1993\) 1225](#).
- [68] S. U. Chung, and J. M. Friedrich, *Covariant helicity-coupling amplitudes: A new formulation*, [Phys. Rev. D **78** \(2008\) 074027](#).
- [69] F. James(CERN), M. Roos(CERN), *Minuit: A system for function minimization and analysis of the parameter errors and correlations*, [Comput. Phys. Commun. **10** \(1975\) 343](#).
- [70] BESII Collaboration, *The σ pole in $J/\psi \rightarrow \omega\pi^+\pi^-$* , [Phys. Lett. B **598** \(2004\) 149](#).
- [71] BESII Collaboration, *Production of σ in $\psi(2S) \rightarrow \pi^+\pi^- J/\psi$* , [Phys. Lett. B **645**, \(2007\) 19](#).
- [72] S. Eidelman and F. Jegerlehner, *Hadronic contributions to $g-2$ of the leptons and to the effective fine structure constant $\alpha(M_z^2)$* , [Z. Phys. C **67** \(1995\) 585 \[hep-ph/9502298\]](#).
- [73] F. Jegerlehner, *Precision measurements of σ_{hadronic} for $\alpha_{\text{eff}}(E)$ at ILC energies and $(g-2)_\mu$* , [Nucl. Phys. B **162** \(2006\) 22-32](#).

- [74] F. Jegerlehner, *The running fine structure constant $\alpha(E)$ via the Adler function*, *Nucl. Phys. Proc. Suppl.* **181** (2008) 135.
- [75] F. Jegerlehner, *Theoretical precision in estimates of the hadronic contributions to $(g - 2)_\mu$ and $\alpha_{QED}(M_Z)$* , *Nucl. Phys. Proc. Suppl.* **126** (2004) 325 [[hep-ph/0310234](#)].
- [76] F. Jegerlehner, *Hadronic vacuum polarization effects in $\alpha_{em}(M_Z)$* , [[hep-ph/0308117v1](#)].
- [77] E. A. Kuraev and V. S. Fadin, *On radiative correction to e^+e^- single photon annihilation at high energy*, *Sov. J. Nucl. Phys.* **41** (1985) 466.
- [78] BESIII Collaboration, *Search for a strangeonium-like structure Z_s decaying into $\phi\pi$ and a measurement of the cross section $e^+e^- \rightarrow \phi\pi\pi$* , *Phys. Rev. D* **99** (2019) 011101.
- [79] BESIII Collaboration, *Branching fraction measurements of χ_{c0} and χ_{c2} to $\pi^0\pi^0$ and $\eta\eta$* , *Phys. Rev. D* **81** (2010) 052005.
- [80] BESIII Collaboration, *Search for hadronic transition $\chi_{cJ} \rightarrow \eta_c\pi^+\pi^-$ and observation of $\chi_{cJ} \rightarrow K\bar{K}\pi\pi\pi$* , *Phys. Rev. D* **87** (2013) 012002.
- [81] BESIII Collaboration, *Luminosity measurements for the R scan experiment at BESIII*, *Chin. Phys. C* **41** (2017) 063001.
- [82] C. P. Shen and C. Z. Yuan, *Combined fit to BABAR and Belle data on $e^+e^- \rightarrow \phi\pi^+\pi^-$ and $\phi f_0(980)$* , *Chin. Phys. C* **34** (2010) 1045-1051.
- [83] BESIII Collaboration, *Precise measurement of the $e^+e^- \rightarrow \pi^+\pi^- J/\psi$ cross section at center-of-mass energies from 3.77 to 4.60 GeV*, *Phys. Rev. Lett.* **118** (2017) 092001.
- [84] S. Eidelman and F. Jegerlehner, *Hadronic contributions to $(g - 2)$ of the leptons and to the effective fine structure constant $\alpha(M_Z^2)$* , *Zeitschrift für Physik C Particles and Fields* **67** (1995) 585-601.

BESIII collaboration

M. Ablikim¹, M. N. Achasov^{10,b}, P. Adlarson⁶⁸, S. Ahmed¹⁴, M. Albrecht⁴, R. Aliberti²⁸, A. Amoroso^{67A,67C}, M. R. An³², Q. An^{64,50}, X. H. Bai⁵⁸, Y. Bai⁴⁹, O. Bakina²⁹, R. Baldini Ferroli^{23A}, I. Balossino^{24A}, Y. Ban^{39,h}, V. Batozskaya^{1,37}, D. Becker²⁸, K. Begzsuren²⁶, N. Berger²⁸, M. Bertani^{23A}, D. Bettoni^{24A}, F. Bianchi^{67A,67C}, J. Bloms⁶¹, A. Bortone^{67A,67C}, I. Boyko²⁹, R. A. Briere⁵, A. Brueggemann⁶¹, H. Cai⁶⁹, X. Cai^{1,50}, A. Calcaterra^{23A}, G. F. Cao^{1,55}, N. Cao^{1,55}, S. A. Cetin^{54A}, J. F. Chang^{1,50}, W. L. Chang^{1,55}, G. Chelkov^{29,a}, C. Chen³⁶, G. Chen¹, H. S. Chen^{1,55}, M. L. Chen^{1,50}, S. J. Chen³⁵, T. Chen¹, X. R. Chen²⁵, X. T. Chen¹, Y. B. Chen^{1,50}, Z. J. Chen^{20,i}, W. S. Cheng^{67C}, G. Cibinetto^{24A}, F. Cossio^{67C}, J. J. Cui⁴², H. L. Dai^{1,50}, J. P. Dai⁷¹, X. C. Dai^{1,55}, A. Dbeyssi¹⁴, R. E. de Boer⁴, D. Dedovich²⁹, Z. Y. Deng¹, A. Denig²⁸, I. Denysenko²⁹, M. Destefanis^{67A,67C}, F. De Mori^{67A,67C}, Y. Ding³³, J. Dong^{1,50}, L. Y. Dong^{1,55}, M. Y. Dong^{1,50,55}, X. Dong⁶⁹, S. X. Du⁷³, P. Egorov^{29,a}, Y. L. Fan⁶⁹, J. Fang^{1,50}, S. S. Fang^{1,55}, Y. Fang¹, R. Farinelli^{24A}, L. Fava^{67B,67C}, F. Feldbauer⁴, G. Felici^{23A}, C. Q. Feng^{64,50}, J. H. Feng⁵¹, K. Fischer⁶², M. Fritsch⁴, C. D. Fu¹, Y. N. Gao^{39,h}, Yang Gao^{64,50}, I. Garzia^{24A,24B}, P. T. Ge⁶⁹, C. Geng⁵¹, E. M. Gersabeck⁵⁹, A. Gilman⁶², K. Goetzen¹¹, L. Gong³³, W. X. Gong^{1,50}, W. Gradl²⁸, M. Greco^{67A,67C}, M. H. Gu^{1,50}, C. Y. Guan^{1,55}, A. Q. Guo²², A. Q. Guo²⁵, L. B. Guo³⁴, R. P. Guo⁴¹, Y. P. Guo^{9,g}, A. Guskov^{29,a}, T. T. Han⁴², W. Y. Han³², X. Q. Hao¹⁵, F. A. Harris⁵⁷, K. K. He⁴⁷,

K. L. He^{1,55}, F. H. Heinsius⁴, C. H. Heinz²⁸, Y. K. Heng^{1,50,55}, C. Herold⁵², M. Himmelreich^{11,e},
 T. Holtmann⁴, G. Y. Hou^{1,55}, Y. R. Hou⁵⁵, Z. L. Hou¹, H. M. Hu^{1,55}, J. F. Hu^{48,j},
 T. Hu^{1,50,55}, Y. Hu¹, G. S. Huang^{64,50}, K. X. Huang⁵¹, L. Q. Huang⁶⁵, X. T. Huang⁴²,
 Y. P. Huang¹, Z. Huang^{39,h}, T. Hussain⁶⁶, N. Hüskén^{22,28}, W. Imoehl²², M. Irshad^{64,50},
 S. Jaeger⁴, S. Janchiv²⁶, Q. Ji¹, Q. P. Ji¹⁵, X. B. Ji^{1,55}, X. L. Ji^{1,50}, Y. Y. Ji⁴², H. B. Jiang⁴²,
 S. S. Jiang³², X. S. Jiang^{1,50,55}, J. B. Jiao⁴², Z. Jiao¹⁸, S. Jin³⁵, Y. Jin⁵⁸, M. Q. Jing^{1,55},
 T. Johansson⁶⁸, N. Kalantar-Nayestanaki⁵⁶, X. S. Kang³³, R. Kappert⁵⁶, M. Kavatsyuk⁵⁶,
 B. C. Ke⁷³, I. K. Keshk⁴, A. Khoukaz⁶¹, P. Kiese²⁸, R. Kiuchi¹, R. Kliemt¹¹, L. Koch³⁰,
 O. B. Kolcu^{54A}, B. Kopf⁴, M. Kuemmel⁴, M. Kuessner⁴, A. Kupsc^{37,68}, M. G. Kurth^{1,55},
 W. Kühn³⁰, J. J. Lane⁵⁹, J. S. Lange³⁰, P. Larin¹⁴, A. Lavania²¹, L. Lavezzi^{67A,67C},
 Z. H. Lei^{64,50}, H. Leithoff²⁸, M. Lellmann²⁸, T. Lenz²⁸, C. Li⁴⁰, C. Li³⁶, C. H. Li³²,
 Cheng Li^{64,50}, D. M. Li⁷³, F. Li^{1,50}, G. Li¹, H. Li^{64,50}, H. Li⁴⁴, H. B. Li^{1,55}, H. J. Li¹⁵,
 H. N. Li^{48,j}, J. L. Li⁴², J. Q. Li⁴, J. S. Li⁵¹, Ke Li¹, L. J Li¹, L. K. Li¹, Lei Li³, M. H. Li³⁶,
 P. R. Li^{31,k,l}, S. X. Li⁹, S. Y. Li⁵³, T. Li⁴², W. D. Li^{1,55}, W. G. Li¹, X. H. Li^{64,50},
 X. L. Li⁴², Xiaoyu Li^{1,55}, Z. Y. Li⁵¹, H. Liang²⁷, H. Liang^{1,55}, H. Liang^{64,50}, Y. F. Liang⁴⁶,
 Y. T. Liang²⁵, G. R. Liao¹², L. Z. Liao^{1,55}, J. Libby²¹, A. Limphirat⁵², C. X. Lin⁵¹,
 D. X. Lin²⁵, T. Lin¹, B. J. Liu¹, C. X. Liu¹, D. Liu^{14,64}, F. H. Liu⁴⁵, Fang Liu¹, Feng Liu⁶,
 G. M. Liu^{48,j}, H. M. Liu^{1,55}, Huanhuan Liu¹, Huihui Liu¹⁶, J. B. Liu^{64,50}, J. L. Liu⁶⁵,
 J. Y. Liu^{1,55}, K. Liu¹, K. Y. Liu³³, Ke Liu¹⁷, L. Liu^{64,50}, M. H. Liu^{9,g}, P. L. Liu¹, Q. Liu⁵⁵,
 S. B. Liu^{64,50}, T. Liu^{9,g}, T. Liu^{1,55}, W. M. Liu^{64,50}, X. Liu^{31,k,l}, Y. Liu^{31,k,l}, Y. B. Liu³⁶,
 Z. A. Liu^{1,50,55}, Z. Q. Liu⁴², X. C. Lou^{1,50,55}, F. X. Lu⁵¹, H. J. Lu¹⁸, J. D. Lu^{1,55},
 J. G. Lu^{1,50}, X. L. Lu¹, Y. Lu¹, Y. P. Lu^{1,50}, Z. H. Lu¹, C. L. Luo³⁴, M. X. Luo⁷²,
 T. Luo^{9,g}, X. L. Luo^{1,50}, X. R. Lyu⁵⁵, Y. F. Lyu³⁶, F. C. Ma³³, H. L. Ma¹, L. L. Ma⁴²,
 M. M. Ma^{1,55}, Q. M. Ma¹, R. Q. Ma^{1,55}, R. T. Ma⁵⁵, X. X. Ma^{1,55}, X. Y. Ma^{1,50}, Y. Ma^{39,h},
 F. E. Maas¹⁴, M. Maggiora^{67A,67C}, S. Maldaner⁴, S. Malde⁶², Q. A. Malik⁶⁶, A. Mangoni^{23B},
 Y. J. Mao^{39,h}, Z. P. Mao¹, S. Marcello^{67A,67C}, Z. X. Meng⁵⁸, J. G. Messchendorp^{56,d},
 G. Mezzadri^{24A}, H. Miao¹, T. J. Min³⁵, R. E. Mitchell²², X. H. Mo^{1,50,55}, N. Yu. Muchnoi^{10,b},
 H. Muramatsu⁶⁰, S. Nakhoul^{11,e}, Y. Nefedov²⁹, F. Nerling^{11,e}, I. B. Nikolaev^{10,b}, Z. Ning^{1,50},
 S. Nisar^{8,m}, S. L. Olsen⁵⁵, Q. Ouyang^{1,50,55}, S. Pacetti^{23B,23C}, X. Pan^{9,g}, Y. Pan⁵⁹, A. Pathak¹,
 A. Pathak²⁷, M. Pelizaeus⁴, H. P. Peng^{64,50}, K. Peters^{11,e}, J. Pettersson⁶⁸, J. L. Ping³⁴,
 R. G. Ping^{1,55}, S. Plura²⁸, S. Pogodin²⁹, R. Poling⁶⁰, V. Prasad^{64,50}, H. Qi^{64,50}, H. R. Qi⁵³,
 M. Qi³⁵, T. Y. Qi^{9,g}, S. Qian^{1,50}, W. B. Qian⁵⁵, Z. Qian⁵¹, C. F. Qiao⁵⁵, J. J. Qin⁶⁵,
 L. Q. Qin¹², X. P. Qin^{9,g}, X. S. Qin⁴², Z. H. Qin^{1,50}, J. F. Qiu¹, S. Q. Qu³⁶, S. Q. Qu⁵³,
 K. H. Rashid⁶⁶, K. Ravindran²¹, C. F. Redmer²⁸, K. J. Ren³², A. Rivetti^{67C}, V. Rodin⁵⁶,
 M. Rolo^{67C}, G. Rong^{1,55}, Ch. Rosner¹⁴, M. Rump⁶¹, H. S. Sang⁶⁴, A. Sarantsev^{29,c}, Y. Schelhaas²⁸,
 C. Schnier⁴, K. Schoenning⁶⁸, M. Scodreggio^{24A,24B}, K. Y. Shan^{9,g}, W. Shan¹⁹, X. Y. Shan^{64,50},
 J. F. Shangguan⁴⁷, L. G. Shao^{1,55}, M. Shao^{64,50}, C. P. Shen^{9,g}, H. F. Shen^{1,55}, X. Y. Shen^{1,55},
 B.-A. Shi⁵⁵, H. C. Shi^{64,50}, R. S. Shi^{1,55}, X. Shi^{1,50}, X. D Shi^{64,50}, J. J. Song¹⁵, W. M. Song^{27,1},
 Y. X. Song^{39,h}, S. Sosio^{67A,67C}, S. Spataro^{67A,67C}, F. Stieler²⁸, K. X. Su⁶⁹, P. P. Su⁴⁷,
 Y.-J. Su⁵⁵, G. X. Sun¹, H. K. Sun¹, J. F. Sun¹⁵, L. Sun⁶⁹, S. S. Sun^{1,55}, T. Sun^{1,55},
 W. Y. Sun²⁷, X Sun^{20,i}, Y. J. Sun^{64,50}, Y. Z. Sun¹, Z. T. Sun⁴², Y. H. Tan⁶⁹, Y. X. Tan^{64,50},
 C. J. Tang⁴⁶, G. Y. Tang¹, J. Tang⁵¹, L. Y Tao⁶⁵, Q. T. Tao^{20,i}, J. X. Teng^{64,50}, V. Thoren⁶⁸,
 W. H. Tian⁴⁴, Y. T. Tian²⁵, I. Uman^{54B}, B. Wang¹, D. Y. Wang^{39,h}, F. Wang⁶⁵, H. J. Wang^{31,k,l},

H. P. Wang^{1,55}, K. Wang^{1,50}, L. L. Wang¹, M. Wang⁴², M. Z. Wang^{39,h}, Meng Wang^{1,55}, S. Wang^{9,g}, T. J. Wang³⁶, W. Wang⁵¹, W. H. Wang⁶⁹, W. P. Wang^{64,50}, X. Wang^{39,h}, X. F. Wang^{31,k,l}, X. L. Wang^{9,g}, Y. D. Wang³⁸, Y. F. Wang^{1,50,55}, Y. Q. Wang¹, Y. Y. Wang^{31,k,l}, Ying Wang⁵¹, Z. Wang^{1,50}, Z. Y. Wang¹, Ziyi Wang⁵⁵, Zongyuan Wang^{1,55}, D. H. Wei¹², F. Weidner⁶¹, S. P. Wen¹, D. J. White⁵⁹, U. Wiedner⁴, G. Wilkinson⁶², M. Wolke⁶⁸, L. Wollenberg⁴, J. F. Wu^{1,55}, L. H. Wu¹, L. J. Wu^{1,55}, X. Wu^{9,g}, X. H. Wu²⁷, Y. Wu⁶⁴, Z. Wu^{1,50}, L. Xia^{64,50}, T. Xiang^{39,h}, H. Xiao^{9,g}, S. Y. Xiao¹, Y. L. Xiao^{9,g}, Z. J. Xiao³⁴, X. H. Xie^{39,h}, Y. G. Xie^{1,50}, Y. H. Xie⁶, Z. P. Xie^{64,50}, T. Y. Xing^{1,55}, C. F. Xu¹, C. J. Xu⁵¹, G. F. Xu¹, Q. J. Xu¹³, S. Y. Xu⁶³, W. Xu^{1,55}, X. P. Xu⁴⁷, Y. C. Xu⁵⁵, F. Yan^{9,g}, L. Yan^{9,g}, W. B. Yan^{64,50}, W. C. Yan⁷³, H. J. Yang^{43,f}, H. X. Yang¹, L. Yang⁴⁴, S. L. Yang⁵⁵, Y. X. Yang^{1,55}, Yifan Yang^{1,55}, Zhi Yang²⁵, M. Ye^{1,50}, M. H. Ye⁷, J. H. Yin¹, Z. Y. You⁵¹, B. X. Yu^{1,50,55}, C. X. Yu³⁶, G. Yu^{1,55}, J. S. Yu^{20,i}, T. Yu⁶⁵, C. Z. Yuan^{1,55}, L. Yuan², S. C. Yuan¹, X. Q. Yuan¹, Y. Yuan¹, Z. Y. Yuan⁵¹, C. X. Yue³², A. A. Zafar⁶⁶, X. Zeng⁶, Y. Zeng^{20,i}, Y. H. Zhan⁵¹, A. Q. Zhang¹, B. L. Zhang¹, B. X. Zhang¹, G. Y. Zhang¹⁵, H. Zhang⁶⁴, H. H. Zhang²⁷, H. H. Zhang⁵¹, H. Y. Zhang^{1,50}, J. L. Zhang⁷⁰, J. Q. Zhang³⁴, J. W. Zhang^{1,50,55}, J. Y. Zhang¹, J. Z. Zhang^{1,55}, Jianyu Zhang^{1,55}, Jiawei Zhang^{1,55}, L. M. Zhang⁵³, L. Q. Zhang⁵¹, Lei Zhang³⁵, P. Zhang¹, Shulei Zhang^{20,i}, X. D. Zhang³⁸, X. M. Zhang¹, X. Y. Zhang⁴², X. Y. Zhang⁴⁷, Y. Zhang⁶², Y. T. Zhang⁷³, Y. H. Zhang^{1,50}, Yan Zhang^{64,50}, Yao Zhang¹, Z. H. Zhang¹, Z. Y. Zhang³⁶, Z. Y. Zhang⁶⁹, G. Zhao¹, J. Zhao³², J. Y. Zhao^{1,55}, J. Z. Zhao^{1,50}, Lei Zhao^{64,50}, Ling Zhao¹, M. G. Zhao³⁶, Q. Zhao¹, S. J. Zhao⁷³, Y. B. Zhao^{1,50}, Y. X. Zhao²⁵, Z. G. Zhao^{64,50}, A. Zhemchugov^{29,a}, B. Zheng⁶⁵, J. P. Zheng^{1,50}, Y. H. Zheng⁵⁵, B. Zhong³⁴, C. Zhong⁶⁵, X. Zhong⁵¹, L. P. Zhou^{1,55}, Q. Zhou^{1,55}, X. Zhou⁶⁹, X. K. Zhou⁵⁵, X. R. Zhou^{64,50}, X. Y. Zhou³², Y. Z. Zhou^{9,g}, A. N. Zhu^{1,55}, J. Zhu³⁶, K. Zhu¹, K. J. Zhu^{1,50,55}, S. H. Zhu⁶³, T. J. Zhu⁷⁰, W. J. Zhu^{9,g}, W. J. Zhu³⁶, Y. C. Zhu^{64,50}, Z. A. Zhu^{1,55}, B. S. Zou¹, J. H. Zou¹

¹ *Institute of High Energy Physics, Beijing 100049, People's Republic of China*

² *Beihang University, Beijing 100191, People's Republic of China*

³ *Beijing Institute of Petrochemical Technology, Beijing 102617, People's Republic of China*

⁴ *Bochum Ruhr-University, D-44780 Bochum, Germany*

⁵ *Carnegie Mellon University, Pittsburgh, Pennsylvania 15213, USA*

⁶ *Central China Normal University, Wuhan 430079, People's Republic of China*

⁷ *China Center of Advanced Science and Technology, Beijing 100190, People's Republic of China*

⁸ *COMSATS University Islamabad, Lahore Campus, Defence Road, Off Raiwind Road, 54000 Lahore, Pakistan*

⁹ *Fudan University, Shanghai 200433, People's Republic of China*

¹⁰ *G.I. Budker Institute of Nuclear Physics SB RAS (BINP), Novosibirsk 630090, Russia*

¹¹ *GSI Helmholtzcentre for Heavy Ion Research GmbH, D-64291 Darmstadt, Germany*

¹² *Guangxi Normal University, Guilin 541004, People's Republic of China*

¹³ *Hangzhou Normal University, Hangzhou 310036, People's Republic of China*

¹⁴ *Helmholtz Institute Mainz, Staudinger Weg 18, D-55099 Mainz, Germany*

- ¹⁵ *Henan Normal University, Xinxiang 453007, People's Republic of China*
- ¹⁶ *Henan University of Science and Technology, Luoyang 471003, People's Republic of China*
- ¹⁷ *Henan University of Technology, Zhengzhou 450001, People's Republic of China*
- ¹⁸ *Huangshan College, Huangshan 245000, People's Republic of China*
- ¹⁹ *Hunan Normal University, Changsha 410081, People's Republic of China*
- ²⁰ *Hunan University, Changsha 410082, People's Republic of China*
- ²¹ *Indian Institute of Technology Madras, Chennai 600036, India*
- ²² *Indiana University, Bloomington, Indiana 47405, USA*
- ²³ *INFN Laboratori Nazionali di Frascati , (A)INFN Laboratori Nazionali di Frascati, I-00044, Frascati, Italy; (B)INFN Sezione di Perugia, I-06100, Perugia, Italy; (C)University of Perugia, I-06100, Perugia, Italy*
- ²⁴ *INFN Sezione di Ferrara, (A)INFN Sezione di Ferrara, I-44122, Ferrara, Italy; (B)University of Ferrara, I-44122, Ferrara, Italy*
- ²⁵ *Institute of Modern Physics, Lanzhou 730000, People's Republic of China*
- ²⁶ *Institute of Physics and Technology, Peace Ave. 54B, Ulaanbaatar 13330, Mongolia*
- ²⁷ *Jilin University, Changchun 130012, People's Republic of China*
- ²⁸ *Johannes Gutenberg University of Mainz, Johann-Joachim-Becher-Weg 45, D-55099 Mainz, Germany*
- ²⁹ *Joint Institute for Nuclear Research, 141980 Dubna, Moscow region, Russia*
- ³⁰ *Justus-Liebig-Universitaet Giessen, II. Physikalisches Institut, Heinrich-Buff-Ring 16, D-35392 Giessen, Germany*
- ³¹ *Lanzhou University, Lanzhou 730000, People's Republic of China*
- ³² *Liaoning Normal University, Dalian 116029, People's Republic of China*
- ³³ *Liaoning University, Shenyang 110036, People's Republic of China*
- ³⁴ *Nanjing Normal University, Nanjing 210023, People's Republic of China*
- ³⁵ *Nanjing University, Nanjing 210093, People's Republic of China*
- ³⁶ *Nankai University, Tianjin 300071, People's Republic of China*
- ³⁷ *National Centre for Nuclear Research, Warsaw 02-093, Poland*
- ³⁸ *North China Electric Power University, Beijing 102206, People's Republic of China*
- ³⁹ *Peking University, Beijing 100871, People's Republic of China*
- ⁴⁰ *Qufu Normal University, Qufu 273165, People's Republic of China*
- ⁴¹ *Shandong Normal University, Jinan 250014, People's Republic of China*
- ⁴² *Shandong University, Jinan 250100, People's Republic of China*
- ⁴³ *Shanghai Jiao Tong University, Shanghai 200240, People's Republic of China*
- ⁴⁴ *Shanxi Normal University, Linfen 041004, People's Republic of China*
- ⁴⁵ *Shanxi University, Taiyuan 030006, People's Republic of China*
- ⁴⁶ *Sichuan University, Chengdu 610064, People's Republic of China*
- ⁴⁷ *Soochow University, Suzhou 215006, People's Republic of China*
- ⁴⁸ *South China Normal University, Guangzhou 510006, People's Republic of China*
- ⁴⁹ *Southeast University, Nanjing 211100, People's Republic of China*
- ⁵⁰ *State Key Laboratory of Particle Detection and Electronics, Beijing 100049, Hefei 230026, People's Republic of China*

- ⁵¹ Sun Yat-Sen University, Guangzhou 510275, People's Republic of China
- ⁵² Suranaree University of Technology, University Avenue 111, Nakhon Ratchasima 30000, Thailand
- ⁵³ Tsinghua University, Beijing 100084, People's Republic of China
- ⁵⁴ Turkish Accelerator Center Particle Factory Group, (A)Istinye University, 34010, Istanbul, Turkey; (B)Near East University, Nicosia, North Cyprus, Mersin 10, Turkey
- ⁵⁵ University of Chinese Academy of Sciences, Beijing 100049, People's Republic of China
- ⁵⁶ University of Groningen, NL-9747 AA Groningen, The Netherlands
- ⁵⁷ University of Hawaii, Honolulu, Hawaii 96822, USA
- ⁵⁸ University of Jinan, Jinan 250022, People's Republic of China
- ⁵⁹ University of Manchester, Oxford Road, Manchester, M13 9PL, United Kingdom
- ⁶⁰ University of Minnesota, Minneapolis, Minnesota 55455, USA
- ⁶¹ University of Muenster, Wilhelm-Klemm-Str. 9, 48149 Muenster, Germany
- ⁶² University of Oxford, Keble Rd, Oxford, UK OX13RH
- ⁶³ University of Science and Technology Liaoning, Anshan 114051, People's Republic of China
- ⁶⁴ University of Science and Technology of China, Hefei 230026, People's Republic of China
- ⁶⁵ University of South China, Hengyang 421001, People's Republic of China
- ⁶⁶ University of the Punjab, Lahore-54590, Pakistan
- ⁶⁷ University of Turin and INFN, (A)University of Turin, I-10125, Turin, Italy; (B)University of Eastern Piedmont, I-15121, Alessandria, Italy; (C)INFN, I-10125, Turin, Italy
- ⁶⁸ Uppsala University, Box 516, SE-75120 Uppsala, Sweden
- ⁶⁹ Wuhan University, Wuhan 430072, People's Republic of China
- ⁷⁰ Xinyang Normal University, Xinyang 464000, People's Republic of China
- ⁷¹ Yunnan University, Kunming 650500, People's Republic of China
- ⁷² Zhejiang University, Hangzhou 310027, People's Republic of China
- ⁷³ Zhengzhou University, Zhengzhou 450001, People's Republic of China
- ^a Also at the Moscow Institute of Physics and Technology, Moscow 141700, Russia
- ^b Also at the Novosibirsk State University, Novosibirsk, 630090, Russia
- ^c Also at the NRC "Kurchatov Institute", PNPI, 188300, Gatchina, Russia
- ^d Currently at Istanbul Arel University, 34295 Istanbul, Turkey
- ^e Also at Goethe University Frankfurt, 60323 Frankfurt am Main, Germany
- ^f Also at Key Laboratory for Particle Physics, Astrophysics and Cosmology, Ministry of Education; Shanghai Key Laboratory for Particle Physics and Cosmology; Institute of Nuclear and Particle Physics, Shanghai 200240, People's Republic of China
- ^g Also at Key Laboratory of Nuclear Physics and Ion-beam Application (MOE) and Institute of Modern Physics, Fudan University, Shanghai 200443, People's Republic of China
- ^h Also at State Key Laboratory of Nuclear Physics and Technology, Peking University, Beijing 100871, People's Republic of China
- ⁱ Also at School of Physics and Electronics, Hunan University, Changsha 410082, China
- ^j Also at Guangdong Provincial Key Laboratory of Nuclear Science, Institute of Quantum Matter, South China Normal University, Guangzhou 510006, China
- ^k Also at Frontiers Science Center for Rare Isotopes, Lanzhou University, Lanzhou 730000,

People's Republic of China

^l *Also at Lanzhou Center for Theoretical Physics, Lanzhou University, Lanzhou 730000,
People's Republic of China*

^m *Also at the Department of Mathematical Sciences, IBA, Karachi , Pakistan*